

# Journal of Geophysical Research: Atmospheres

## RESEARCH ARTICLE

10.1002/2016JD025333

**Key Points:**

- The predicted DMS spatial distribution and sulfur budgets are similar to observations
- La Niña winds increase DMS emissions in the tropical Pacific region
- Modeled DMS, aerosols, and clouds suggest a weak positive feedback on sea surface temperature at interannual timescales

**Supporting Information:**

- Supporting Information S1

**Correspondence to:**

L. M. Russell,  
lmrussell@ucsd.edu

**Citation:**

Xu, L., P. Cameron-Smith, L. M. Russell, S. J. Ghan, Y. Liu, S. Elliott, Y. Yang, S. Lou, M. A. Lamjiri, and M. Manizza (2016), DMS role in ENSO cycle in the tropics, *J. Geophys. Res. Atmos.*, 121, 13,537–13,558, doi:10.1002/2016JD025333.

Received 7 MAY 2016

Accepted 25 OCT 2016

Accepted article online 28 OCT 2016

Published online 16 NOV 2016

## DMS role in ENSO cycle in the tropics

Li Xu<sup>1,2</sup>, Philip Cameron-Smith<sup>3</sup>, Lynn M. Russell<sup>1</sup>, Steven J. Ghan<sup>4</sup>, Ying Liu<sup>4</sup>, Scott Elliott<sup>5</sup>, Yang Yang<sup>1,4</sup>, Sijia Lou<sup>1,4</sup>, Maryam A. Lamjiri<sup>1</sup>, and Manfredi Manizza<sup>1</sup>

<sup>1</sup>Scripps Institution of Oceanography, University of California, San Diego, La Jolla, California, USA, <sup>2</sup>Now at Department of Earth System Science, University of California, Irvine, California, USA, <sup>3</sup>Atmospheric, Earth and Energy Division, Lawrence Livermore National Laboratory, Livermore, California, USA, <sup>4</sup>Atmospheric Science and Global Change Division, Pacific Northwest National Laboratory, Richland, Washington, USA, <sup>5</sup>Climate Ocean Sea Ice Modeling, Los Alamos National Laboratory, Los Alamos, New Mexico, USA

**Abstract** We examined the multiyear mean and variability of dimethyl sulfide (DMS) and its relationship to sulfate aerosols, as well as cloud microphysical and radiative properties. We conducted a 150 year simulation using preindustrial conditions produced by the Community Earth System Model embedded with a dynamic DMS module. The model simulated the mean spatial distribution of DMS emissions and burden, as well as sulfur budgets associated with DMS, SO<sub>2</sub>, H<sub>2</sub>SO<sub>4</sub>, and sulfate that were generally similar to available observations and inventories for a variety of regions. Changes in simulated sea-to-air DMS emissions and associated atmospheric abundance, along with associated aerosols and cloud and radiative properties, were consistently dominated by El Niño–Southern Oscillation (ENSO) cycle in the tropical Pacific region. Simulated DMS, aerosols, and clouds showed a weak positive feedback on sea surface temperature. This feedback suggests a link among DMS, aerosols, clouds, and climate on interannual timescales. The variability of DMS emissions associated with ENSO was primarily caused by a higher variation in wind speed during La Niña events. The simulation results also suggest that variations in DMS emissions increase the frequency of La Niña events but do not alter ENSO variability in terms of the standard deviation of the Niño 3 sea surface temperature anomalies.

### 1. Introduction

Dimethyl sulfide (DMS), the main natural source of tropospheric biogenic sulfur, is released from the ocean surface and then oxidized in the atmosphere to form particle sulfate. DMS contributes to cloud condensation nuclei (CCN) that can alter cloud microphysical properties, thus modulating cloud albedo [Twomey, 1974] and cloud lifetime [Albrecht, 1989] in ocean-influenced regions. Intensive research activities into DMS-aerosol-cloud-climate interactions have been carried out since the formulation of the Charlson-Lovelock-Andreae-Warren (CLAW) hypothesis [Charlson et al., 1987]. The CLAW hypothesis proposes that an increase in DMS fluxes could influence cloud formation to result in brighter clouds with longer cloud lifetimes and, thus, could counteract the warming of Earth's climate system. To date, the CLAW hypothesis has not been confirmed by conclusive evidence. Some previous studies have rejected the concept of climate regulation through this mechanism on global scales and long time scales [Wolff et al., 2006; Vallina et al., 2007; Kloster et al., 2006]. Others have questioned the strength and extent of the hypothesized feedback [Woodhouse et al., 2010; Quinn and Bates, 2011]. On the other hand, some recent global studies support the DMS-sulfate-climate feedback [Vallina and Simó, 2007; Gabric et al., 2013; Six et al., 2013]. Owing to the complexity of the DMS cycle and the uncertainties involved in each step of the proposed feedback loop (including DMS air-sea exchange to DMS oxidation to form sulfate; sulfate aerosol contribution to CCN; CCN influence on cloud microphysics and, hence, cloud albedo and lifetimes; cloud influence on climate change; and climate feedback on DMS production), the link between DMS and associated sulfur, clouds, and climate is still poorly understood [Harvey, 2007; Vogt and Liss, 2009].

Presently, many climate science studies focus on anthropogenic activities and their impacts on climate, with few considering the impacts from natural forcing—which could have similar contributions to climate change as anthropogenic forcing. Carslaw et al. [2013] suggested that much (45%) of the uncertainty in aerosol indirect forcing since 1750 (the preindustrial era) is from uncertainties in emissions of natural aerosols, including sea salt, volcanic sulfur dioxide, marine dimethyl sulfide, biogenic volatile organic carbon, and biomass burning; only 34% is from uncertainty in anthropogenic emissions. Furthermore, Carslaw et al. [2013]

found that one of the largest contributions of natural aerosol emissions to forcing uncertainties was the CCN response to variation in DMS emissions. Their simulations showed that there was a 44% higher susceptibility of CCN to DMS during summertime in the preindustrial (PI) era compared to present-day (PD) measurements; this difference resulted from the more efficient nucleation of new particles in the cleaner PI atmosphere. This result from the Carslaw study highlights the importance of understanding the role of DMS and its associated sulfate aerosols, especially during the preindustrial era.

Observations clearly show that atmospheric DMS shows the same seasonal cycle as aerosol-phase non-sea-salt sulfate at Cape Grim, Tasmania [Ayers *et al.*, 1991], above an Antarctic coastal site [Preunkert *et al.*, 2007], and during a summertime cruise in the northwestern Pacific [Ooki *et al.*, 2003]. Moreover, atmospheric DMS shows similar seasonal CCN cycles at Cape Grim, Tasmania [Ayers and Gras, 1991], and at the Mace Head Irish coastal site [Reade *et al.*, 2006]. Two modeling studies [Gabric *et al.*, 2002; Vallina *et al.*, 2007] show a significant contribution of DMS-derived CCN to total CCN, which agrees with the DMS-CCN link proposed by the CLAW hypothesis. In addition, ocean biological productivity was strongly influenced by interannual variations in the tropical Pacific [Chavez *et al.*, 1998, 1999; Leonard and McClain, 1996]. Specifically, phytoplankton typically blooms in the eastern equatorial Pacific during La Niña because of greater oceanic upwelling over the region, while blooms are less productive during El Niño. The transition between El Niño and La Niña results in interannual variations of DMS emissions produced by phytoplankton. In contrast, Bates and Quinn [1997] showed that surface seawater DMS concentration had no evidence of interannual variation in atmospheric and oceanic properties associated with El Niño–Southern Oscillation (ENSO) events. On the other hand, when phytoplankton in the upper ocean absorb sunlight via photosynthesis, they may influence ENSO variability [Lewis *et al.*, 1990] by changing the equatorial Pacific heat budget; this leads to a change in solar heating and, hence, a change in sea surface temperature. Along with an increase in chlorophyll concentration resulting from increased phytoplankton productivity, a decrease in ENSO amplitude has been reported in several modeling studies [Timmermann and Jin, 2002; Wetzel *et al.*, 2006; Zhang *et al.*, 2009; Jochum *et al.*, 2010] but others report an increase [Marzeion *et al.*, 2005; Lengaigne *et al.*, 2007; Anderson *et al.*, 2007; Ballabrera-Poy *et al.*, 2007; Löptien *et al.*, 2009]. These debates have been based on either a statistically representative atmosphere coupled to an ocean general circulation model (GCM) with a simple temperature-chlorophyll relationship or have been based on coupled general circulation models with full ecosystems that neglect the DMS cycle. Thus, a study using a state-of-the-art global climate model with full ecosystems embedded that include an up-to-date dynamic DMS mechanism can be used to improve our understanding of the interaction among DMS, aerosols, clouds, and climate.

The objective of this study is to investigate the interannual variability of DMS and associated aerosols and their effects on Earth's climate. In recognition of the influence of the preindustrial variability of DMS emissions on variations in radiative forcing, we conducted a 150 year simulation for preindustrial conditions (year 1850 emissions) using the Community Earth System Model (CESM) [Hurrell *et al.*, 2013]. This simulation, with interactive DMS emissions, allowed us to assess the impacts of DMS emissions on associated aerosols and cloud properties. In addition, by comparing the simulation with another simulation using prescribed climatological monthly DMS emissions, we explored the extent to which DMS variation can contribute to modulating ENSO variability in the tropical Pacific.

This paper is organized as follows. The CESM model is briefly described in section 2, with a focus on aspects of the model that are relevant to DMS emissions and the associated marine aerosols. Analysis of the sulfur budget associated with DMS,  $\text{SO}_2$ ,  $\text{H}_2\text{SO}_4$ , and sulfate aerosols, along with an investigation of DMS variability and its associated aerosol and cloud variability, is presented in section 3. Discussion and conclusions are addressed in section 4.

## 2. Model

The 150 year simulation for preindustrial conditions was performed using the Community Earth System Model (CESM), which is composed of atmosphere, ocean, land surface, and sea ice components [Hurrell *et al.*, 2013]. The specific version was an enhanced version of CESM version 1.2.2. The Parallel Ocean Program (POP) is the ocean general circulation model that incorporates a carbon/nitrogen/silicon/iron ocean ecosystem model with distinguished classes of phytoplankton (e.g., diatoms, coccolithophores, diazotrophs, and collective picoplankton) [Moore *et al.*, 2004]. The DMS mechanism uses a high-sulfur producer,

Phaeocystis [Elliott, 2009]. Details about the representation of DMS and the oceanic ecosystem can be found in Cameron-Smith *et al.* [2011] and Elliott [2009]. The coupled model utilizes a superfast chemistry mechanism with interactive atmospheric chemistry developed at the Lawrence Livermore National Lab [Lamarque *et al.*, 2012; Cameron-Smith *et al.*, 2006]. The model uses a modal aerosol module (MAM3) with three size classes, including the Aitken mode (dry diameter size range of 0.02–0.08  $\mu\text{m}$ ), accumulation mode (0.08–1.0  $\mu\text{m}$ ), and coarse mode (1.0–10.0  $\mu\text{m}$ ). For each mode, the model calculates mass mixing ratios of internally mixed aerosol components and the total number mixing ratio. Six aerosol components (sulfate, sea salt, mineral dust, black carbon, primary organic matter, and secondary organic matter) are included in MAM3. MAM3 handles the complex aerosol physical, chemical and optical properties (e.g., number/mass concentration, size, density, refractive index, and chemical composition) and numerous aerosol processes in the atmosphere (e.g., aerosol emissions, nucleation, coagulation, condensational growth, gas- and aqueous-phase chemistry, dry and wet deposition, gravitational settling, and water uptake) and was evaluated in detail by Liu *et al.* [2012].

Parameterizations are as follows: Surface emission of sea-salt small particles (diameter  $<2.8 \mu\text{m}$ ) follows the method of Mårtensson *et al.* [2003], while larger particles (diameter  $>2.8 \mu\text{m}$ ) follow the method of Monahan *et al.* [1986]. Dust aerosols are emitted in both accumulation and coarse modes, according to the dust entrainment and deposition model developed by Zender *et al.* [2003]. DMS emission is based on the simulated ocean DMS concentration and a transfer velocity as a function of 10 m wind speed following Elliott [2009]. Once in the atmosphere, DMS can be rapidly oxidized by free radicals such as OH, NO<sub>3</sub>, BrO, and O<sub>3</sub> to form non-sea-salt sulfate and/or MSA. In this simulation, only the DMS oxidation pathway with OH was used. Volcanic sulfur in the model is emitted as 97.5% SO<sub>2</sub> and 2.5% primary sulfate aerosol based on the year 1850 [Dentener *et al.*, 2006]. The atmosphere model resolution is 1.9° latitude by 2.5° longitude in the horizontal, with 30 vertical layers ranging from the surface to 3.6 hPa. The model treats stratiform clouds using detailed microphysics schemes described by Morrison and Gettelman [2008]. Treatments of deep and shallow convective cloud parameterizations are described in Zhang and McFarlane [1995] and Park and Bretherton [2009], respectively. More detailed cloud processes in CAM5 appear in Park *et al.* [2014]. The model containing interactive DMS emission fluxes (i.e., the simulation we call IDMS) was integrated over 150 years. We disregarded 10 years for spin-up of the surface ocean, and results from years 11–150 were used in this study.

In addition to assessing feedback from variations of DMS emission flux on climate variability, we conducted an alternative 150 year simulation with prescribed climatological monthly DMS fluxes [Dentener *et al.*, 2006] (i.e., the simulation we call PDMS); results from years 11–150 were used. Variables used for analyzing this work were saved as monthly averages. The chemistry module in the PDMS simulation was not identical to that in the IDMS simulation. The chemical reactions included in the PDMS simulation differed slightly from those included in the IDMS simulation since the simulations had been designed for different purposes and this direct comparison was not foreseen. The difference in the chemistry mechanism relevant to DMS between the PDMS and IDMS simulations is that the PDMS simulation includes DMS oxidation with both OH and nitrate but the IDMS simulation includes only the daytime pathway (i.e., DMS + OH) but not the nighttime pathway (i.e., DMS + NO<sub>3</sub>). This difference may have contributed to the different mean atmospheric DMS abundance values but is likely to have had a small effect on the variability investigated here. Since the major focus of this work is to investigate the interannual variability of DMS, we addressed this by calculating anomalies, i.e., subtracting climatological monthly mean values before comparing results between the IDMS and PDMS simulations, unless otherwise specified.

### 3. Results

#### 3.1. Atmospheric DMS Flux and Burden

Figure 1 shows the IDMS simulation using a 140 year climatological annual mean and standard deviation of DMS emissions (a, b) and atmospheric burden (c, d), respectively. Relatively high DMS fluxes (Figure 1a) were located over regions with persistent high wind speed (e.g., the broadband between 40°S and 60°S over the Southern Ocean and the storm track regions over the North Pacific) and in regions over the equatorial Pacific and Atlantic Ocean where sea surface DMS concentration was high. The overall spatial distribution of annual mean DMS emission fluxes is in accordance with Dentener *et al.* [2006] and Kloster *et al.* [2006]. Higher standard deviation values (Figure 1b) are colocated with the highest mean DMS

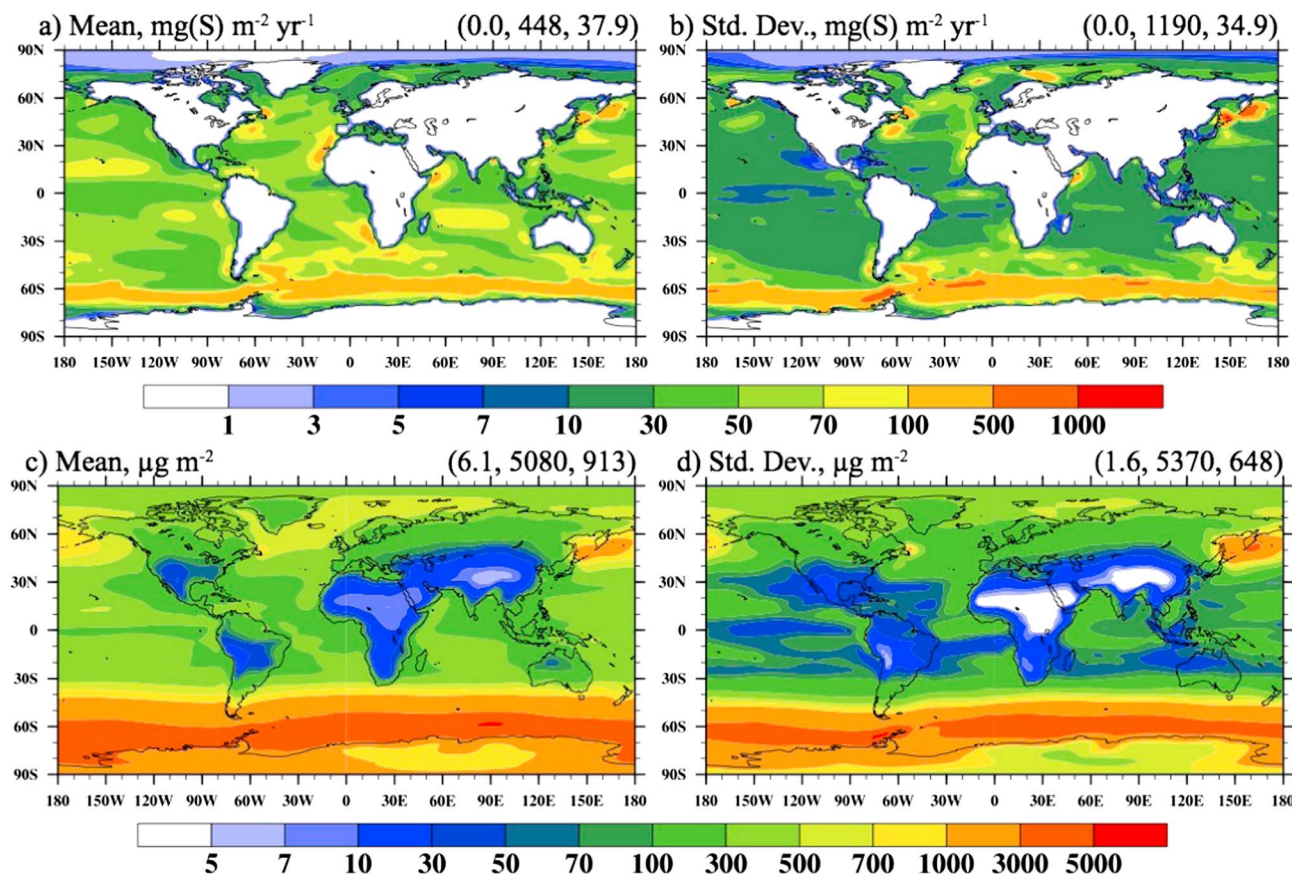


**Figure 1.** Climatological mean and standard deviation of (a, b) DMS emission ( $\text{mg}(\text{S}) \text{ m}^{-2} \text{ yr}^{-1}$ ) and (c, d) DMS burden ( $\mu\text{g m}^{-2}$ ) from the IDMS simulation. The global minimum, maximum, and average values are shown in the upper right corner of each panel.

emission fluxes, especially over the Southern Ocean and North Pacific Ocean, where standard wind speed variation was greater. The highest mean atmospheric DMS abundance (Figure 1c) is located in regions with high DMS emissions (e.g., the Southern Hemisphere around 60°S and storm track regions over the North Pacific). Due to high OH concentrations in the equatorial Pacific and Atlantic Ocean, the DMS burden is not pronounced even though DMS emission fluxes are high. The average column-integrated DMS burden ranges from 6 to 5080  $\mu\text{g m}^{-2}$ , with a mean of 913  $\mu\text{g m}^{-2}$ . The DMS burden over the broadband of the Southern Ocean (40°S–60°S), which has mean values ranging from 3000 to 5000  $\mu\text{g m}^{-2}$ , is significantly higher than roughly 600  $\mu\text{g m}^{-2}$  that was found by Kloster *et al.* [2006]. This discrepancy is mainly due to the higher DMS emissions in this region that were employed by Kloster *et al.* [2006]. As shown in Figure 1, the highest standard deviation of atmospheric DMS burden agrees with high mean values simulated in those regions.

In Figure 2, we compare model results with three sets of atmospheric DMS surface concentrations measured during the Southern Hemisphere Marine Aerosol Characterization Experiment (ACE-1) [Bates *et al.*, 1998] and two sets of atmospheric DMS surface concentrations in the Pacific Ocean, one from May to July 2004 [Marandino *et al.*, 2007] and the other from January 2006 [Marandino *et al.*, 2009]. Figure 2a shows the locations of these measurements. Figure 2b shows field measurements with temporal coverage ranging from 21 October 1995 to 12 December 1995, while Figures 2e and 2f show measurements from Cape Grim and Macquarie Island with temporal coverage from 16 October 1995 to 13 December 1995 and from 25 September 1995 to 3 January 1996, respectively. For the purpose of the intercomparison of the IDMS run, we include modeled climatological mean atmospheric DMS surface concentrations from the PDMS simulation with prescribed monthly DMS emission fluxes by Kettle and Andreae [2000], which were readily available and had been well tested by Liu *et al.* [2012] before we started our simulations.

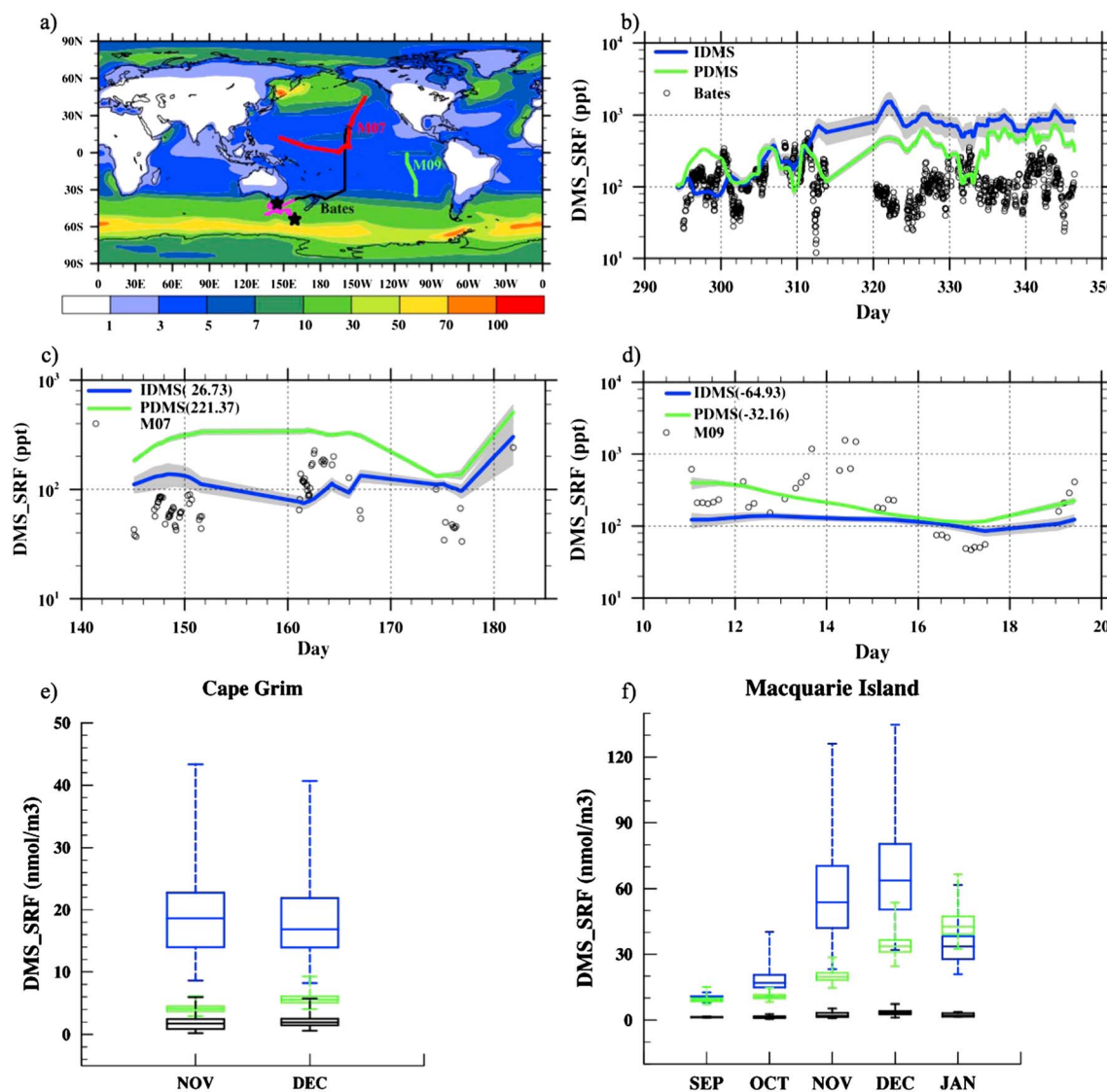


**Figure 2.** (a) Climatological annual mean modeled atmospheric surface DMS concentration ( $\text{nmol m}^{-3}$ ) from the simulation with the interactive DMS emission flux (i.e., IDMS). The polylines and marker depict locations of in situ measured atmospheric DMS surface concentrations. Two black stars represent Cape Grim and Macquarie Island, while the solid black line represents the locations taken in the ACE-1 campaign by Bates and coworkers (labeled as Bates) [Bates et al., 1998]. Note that the magenta lines stand for the measurements taken after the day 312 where modeled values start deviating from the observed ones. The red and green lines stand for locations of measurements in the Pacific Ocean from May to July in 2004 (labeled as M07) [Marandino et al., 2007] and on January in 2006 (labeled as M09) [Marandino et al., 2009], respectively. (b) Time series of measured DMS concentration by Bates (black circle) and mean modeled DMS surface concentrations from the IDMS simulation (blue line) and from the simulation with the prescribed DMS (i.e., PDMS) emission flux (green line). The gray shaded area stands for the standard deviation of corresponding modeled DMS surface concentrations. (c) Same as Figure 2b but for time series of measured DMS concentration by Marandino et al. [2007] (black circle). The value in the parentheses represents the average percentage difference from observations (%). (d) Same as Figure 2c but for time series of measured DMS concentration by Marandino et al. [2007] (black circle). (e) Boxplot of modeled (blue for IDMS and green for PDMS) and observed (black) DMS surface concentrations in Cape Grim. (f) Box plots of modeled (blue for IDMS and green for PDMS) and observed (black) DMS surface concentrations in Macquarie Island.

As shown in Figure 2b, both simulations captured measured DMS surface concentrations over the central Pacific from  $40^{\circ}\text{S}$  to  $20^{\circ}\text{N}$  (i.e., Figure 2a, black line). However, south of  $40^{\circ}\text{S}$  (Figure 2a), both models significantly overestimated measured DMS concentrations by a factor of approximately 5–10 (Figure 2b) at Cape Grim (Figure 2e) and by a factor of 2–10 at Macquarie Island (Figure 2f). Modeled DMS surface concentrations agree with those measured within a factor of 2 over the central and northern Pacific Ocean (Figure 2a, red line) and over the southern Pacific Ocean (Figure 2a, green line). However, the PDMS simulation was 33% closer to the observations than the IDMS one over the southern Pacific Ocean (Figure 2a, green line), while the IDMS simulation shows roughly a factor of 10 smaller model biases than

the PDMS one over the central and northern Pacific Ocean (Figure 2a, red line). The IDMS simulations reproduced variations in seasonal atmospheric DMS surface concentration at Macquarie Island, with the highest phytoplankton blooms in December (during austral summer). In the PDMS simulation, the highest surface concentration of atmospheric DMS did not occur in December but is closer to observations in all three sets of measurements. This large discrepancy between modeled atmospheric DMS surface concentrations in the IDMS simulation and observations over the Southern Ocean is similar to that identified by Elliott [2009], who attributed the bias to the phytoplankton *Phaeocystis* and its high sulfur emissions. Note that results discussed in the following section are based on IDMS simulations where not otherwise noted.

### 3.2. Sulfur Budget

Sulfur transfer, specifically DMS, from the ocean surface to the marine atmosphere is of substantial importance to the sulfur budget of the Earth system. Table 1 summarizes the simulated sulfur budget associated with DMS,  $\text{SO}_2$ ,  $\text{H}_2\text{SO}_4$ , and sulfate aerosols, as well as values provided by previous studies. The values given in previous studies are all present-day conditions. Using the sea-air exchange parameterization of Elliott [2009], the model produced global DMS fluxes of  $22.1 \text{ Tg Syr}^{-1}$  (Table 1). The total DMS emission rate in this work is higher than that reported by Liu *et al.* [2012] ( $18.2 \text{ Tg Syr}^{-1}$ ) and lower than that shown by Kloster *et al.* [2006] ( $27.6 \text{ Tg Syr}^{-1}$ ), though it fell within the ranges of  $15\text{--}33 \text{ Tg Syr}^{-1}$  [Kettle and Andreae, 2000] and  $20\text{--}31 \text{ Tg Syr}^{-1}$  [Le Clainche *et al.*, 2010]. Overall, our simulated global annual mean DMS emission flux into the atmosphere agrees with the PDMS simulation and with previous studies. Our modeled global annual mean DMS burden was about  $0.18 \text{ Tg S}$ , which was in accordance with  $0.20 \text{ Tg S}$  from the PDMS simulation and  $0.17 \text{ Tg S}$  [Gondwe *et al.*, 2003, Table 1]. Given the global mean source of DMS in our model (about  $22 \text{ Tg Syr}^{-1}$  in our IDMS model), the lifetime is about 3 days, a little shorter than the 4 days in the PDMS simulation. Compared with the IDMS simulation, the 32% longer DMS lifetime in the PDMS simulation resulted from the 11% higher DMS burden. The 18% smaller DMS sinks may be attributed to the lack of nighttime DMS oxidation in the IDMS run that is described in section 2. The DMS lifetime is longer than the 1.1 days estimated by Boucher *et al.* [2003] in their EXP1. We also calculated average DMS emission fluxes and burden in both Northern and Southern Hemispheres. The fraction of DMS emission and burden in the southern hemisphere (i.e.,  $90^\circ\text{S}\text{--}0$ ) was 65.7% and 77.8%, respectively, in accordance with 64.5% and 72.7% shown by Kloster *et al.* [2006], although there is the large discrepancy in both DMS emissions and burden over the Southern Ocean (i.e., the broad latitude bands between  $40^\circ\text{S}$  and  $60^\circ\text{S}$ ) described above.

The total IDMS-simulated  $\text{SO}_2$  emission ( $30.2 \text{ Tg Syr}^{-1}$ ) is composed of 52% from DMS oxidation and the remainder from volcanic eruptions. The  $\text{SO}_2$  sinks in the simulation include dry and wet deposition, aqueous-phase oxidation by  $\text{H}_2\text{O}_2$  and  $\text{O}_3$ , and gas-phase oxidation. The model used in this work does not include  $\text{SO}_2$  uptake to sea salt even though previous studies have shown that uptake of  $\text{SO}_2$  to sea salt is a major sink for  $\text{SO}_2$  in the marine boundary layer [Chameides and Stelson, 1992; Pandis *et al.*, 1994; Russell *et al.*, 1994]. The chemical conversion by aqueous-phase and gas-phase oxidation removes 48% of  $\text{SO}_2$ , while dry and wet deposition account for 51% of total removal. We find 33% of total sinks of  $\text{SO}_2$  result from aqueous-phase oxidation, of which 62% is from oxidation by  $\text{H}_2\text{O}_2$ . The global burden of  $\text{SO}_2$  is  $0.16 \text{ Tg S}$  with a lifetime of 1.9 days, which agrees with the 1.6 day lifetime found by Liu *et al.* [2012] and falls within the range (0.6–2.6 days) given by Liu *et al.* [2005]. The production of  $\text{H}_2\text{SO}_4$  gas is through the gas-phase oxidation of  $\text{SO}_2$  by OH. Losses of  $\text{H}_2\text{SO}_4$  (gas) are primarily from condensation onto preexisting particles (94%) and aqueous-phase uptake by cloud water (4%), while a negligible amount is due to nucleation to form new particles and dry deposition (2% in total). The global burden of  $\text{H}_2\text{SO}_4$  is roughly  $0.0003 \text{ Tg S}$ , with a lifetime of 35 min, which is longer than the 14 min reported by Kloster *et al.* [2006] and the 14.5 min reported by Liu *et al.* [2012]. The longer lifetime of  $\text{H}_2\text{SO}_4$  in preindustrial conditions is likely due to the lower particle surface area that is available for  $\text{H}_2\text{SO}_4$  to condense on. The estimated total sulfate aerosol source of  $15.1 \text{ Tg S}$  is primarily produced from aqueous-phase  $\text{SO}_2$  oxidation and from  $\text{H}_2\text{SO}_4$  condensation onto preexisting aerosol and, to a lesser extent, from primary emission (2%) and nucleation. The global burden of sulfate aerosol is  $0.14 \text{ Tg S}$ , with a lifetime of 3.4 days, which falls approximately in the lower end of the range (3.4–4.9 days) given by Textor *et al.* [2006]. The global sources, burden, and lifetime of sulfate aerosols found in this work for preindustrial conditions agree with the values of  $15.2 \text{ Tg Syr}^{-1}$ ,  $0.17 \text{ Tg S}$ , and 4.1 days, respectively, reported by Wang *et al.* [2011]. The dominant sink of sulfate aerosol is wet deposition, which accounts for 88% of the total loss.

**Table 1.** Global Annual Budgets for DMS, SO<sub>2</sub>, H<sub>2</sub>SO<sub>4</sub> and Sulfate Simulated in the IDMS and PDMS Model<sup>a</sup>

	This Work (1850)	Previous Studies (~2000)
<b>DMS</b>		
Sources	22.11; 18.24 <sup>b</sup>	
Emission	22.11(7.58;14.53) <sup>c</sup> ; 18.24 <sup>b</sup>	15–33 <sup>d</sup>
Sinks	22.27; 18.38 <sup>b</sup>	
Gas-phase oxidation	22.27; 18.38 <sup>b</sup>	15–33 <sup>d</sup>
Burden	0.18(0.04;0.14) <sup>c</sup> ; 0.20 <sup>b</sup>	0.084 <sup>e</sup> ~ 0.17 <sup>f</sup>
Lifetime (days)	3.03; 4.0 <sup>b</sup>	0.5–3.0 <sup>g,h</sup>
<b>SO<sub>2</sub></b>		
Sources	30.19	
Emission	14.53	
DMS oxidation	15.65	10.0–24.7 <sup>g,h</sup>
Sinks	30.19	
Dry deposition	6.01	16.0–55.0 <sup>g,h</sup>
Wet deposition	9.48	0.0–19.9 <sup>g,h</sup>
Aqueous-phase oxidation	10.00	6.1–16.8 <sup>g,h</sup>
Gas-phase oxidation	4.70	24.5–57.8 <sup>g,h</sup>
Burden	0.16	0.20–0.61 <sup>g,h</sup>
Lifetime (days)	1.89	0.6–2.6 <sup>g,h</sup>
<b>H<sub>2</sub>SO<sub>4</sub></b>		
Sources	4.70	6.1 ~ 22.0 <sup>g,h</sup>
Gas-phase oxidation	4.70	
Sinks	4.70	
Dry deposition	0.001	
Aqueous-phase uptake	0.19	
Nucleation	0.04	
Condensation	4.42	
Burden	0.0003	
Lifetime (minutes)	35	14.5 <sup>h</sup> ;14.0 <sup>i</sup>
<b>SO<sub>4</sub><sup>2-</sup> (p)</b>		
Sources	15.07	15.24 <sup>j</sup>
Emission	0.37	
SO <sub>2</sub> aqueous-phase oxidation	10.00	
From H <sub>2</sub> O <sub>2</sub> chemistry (%)	62.46	
H <sub>2</sub> SO <sub>4</sub> aqueous-phase uptake	0.19	
H <sub>2</sub> SO <sub>4</sub> nucleation	0.04	
H <sub>2</sub> SO <sub>4</sub> condensation	4.47	
Sinks	15.10	
Dry deposition	1.76	
Wet deposition	13.34	
Burden	0.14	0.17 <sup>j</sup>
Lifetime (days)	3.37	3.38–4.86 <sup>k</sup>

<sup>a</sup>Units are sources and sinks, Tg Syr<sup>-1</sup>; burden, Tg S; lifetime, days except for H<sub>2</sub>SO<sub>4</sub> (minutes).<sup>b</sup>The values behind the semicolon represent values from the PDMS simulation.<sup>c</sup>The values in the parentheses stand for average values in Northern Hemisphere and Southern Hemisphere.<sup>d</sup>Kettle and Andreae [2000].<sup>e</sup>Boucher et al. [2003].<sup>f</sup>Gondwe et al. [2003].<sup>g</sup>Liu et al. [2005].<sup>h</sup>Liu et al. [2012].<sup>i</sup>Kloster et al. [2006].<sup>j</sup>Wang et al. [2011].<sup>k</sup>Textor et al. [2006].

### 3.3. Interannual Variability of DMS and Its Associated Aerosols and Cloud and Radiative Effects

Figures 3a and 3b show a latitude versus time plot of climatological monthly mean atmospheric DMS surface concentration (nmol/m<sup>3</sup>) from the IDMS and PDMS simulations, respectively. Both models produced large variations in DMS during spring and summer seasons at middle-to-high northern (30°N–90°N) and southern latitudes (30°S–90°S), separated by weak variations in the tropics (30°S–30°N). These three distinct seasonal regimes agreed with dynamic DMS models and observations reported by Le Clainche et al. [2010]. In addition,

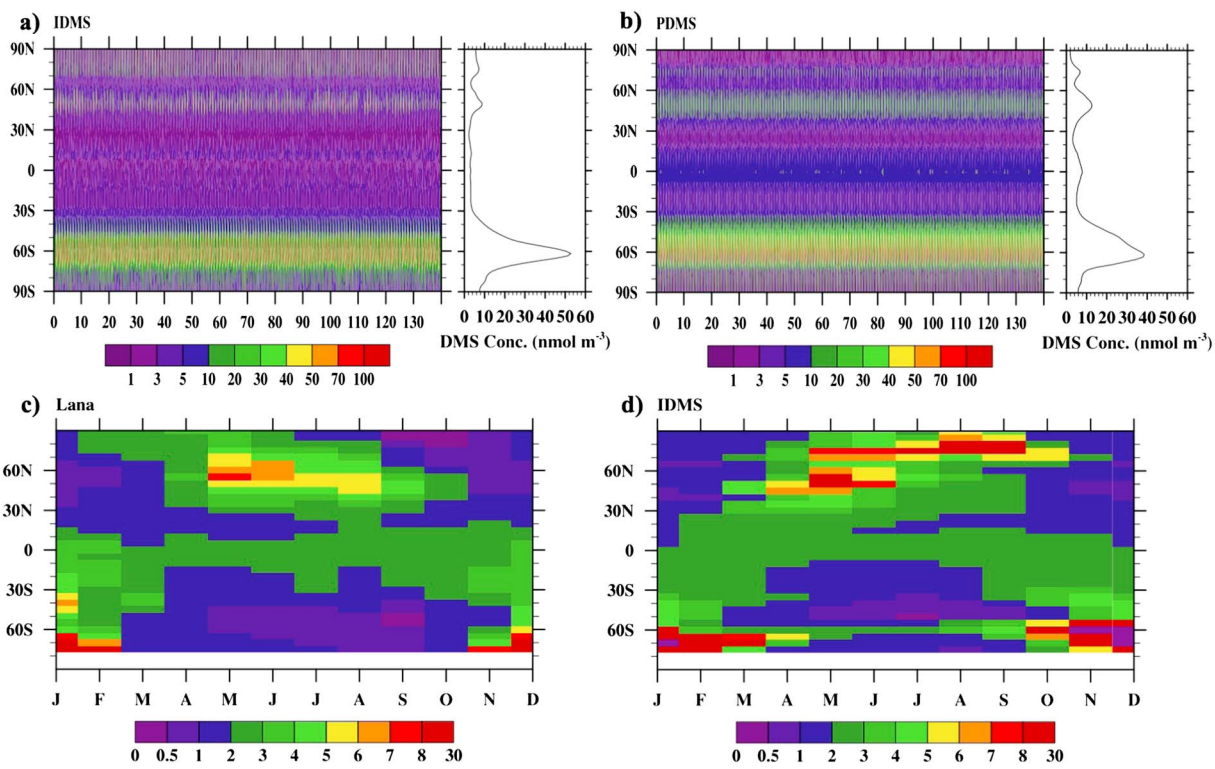


**Figure 3.** Latitude versus time of monthly mean atmospheric DMS concentration ( $\text{nmol m}^{-3}$ ) from the (a) IDMS and (b) PDMS simulation along with their respective zonal mean profile averaged over a 140 year period and climatological monthly mean seawater DMS concentration ( $\mu\text{mol m}^{-3}$ ) from (c) the Lana's climatology [Lana et al., 2011] and (d) the IDMS simulation.

the IDMS model (Figure 3d) captures the seasonal variations of seawater DMS climatology (Figure 3c) described by *Lana et al.* [2011], although the simulated emissions over the Southern Ocean and Northern Hemisphere high latitudes are higher than the observations. The prognostic DMS emission model [Elliott, 2009] used in this study was the best model at capturing the shift from a positive seasonal correlation between phytoplankton bloom and DMS concentration at middle-to-high latitudes and negative correlation at low-to-middle latitudes in the intercomparison by *Le Clainche et al.* [2010], providing high confidence that the interannual variability of DMS and its effects on aerosols and clouds are simulated realistically, especially over the lower (tropical) latitudes.

In order to investigate the interannual variability of DMS, its associated aerosols, and cloud and radiative properties, we used an empirical orthogonal function (EOF) analysis of the monthly anomalies of the relevant variables. The EOF analysis is an effective tool to reveal characteristics of spatial and temporal variability by decomposing simulated variables into a set of orthogonal spatial and temporal patterns. We present here only the leading EOF mode, which represents the highest variance of investigated variables. We also utilized spectral analysis to identify potential periodicities in the leading EOF principal component (PC) over three distinct regions (i.e., middle-to-high northern latitudes, tropics, and middle-to-high southern latitudes) and the entire world. Both the EOF method and spectral analysis are described by *Wilks* [2011].

Figures 4a–4d show the power spectra of the leading mode EOF PC of yearly anomalies of sea surface temperature (SST), DMS emission fluxes (SFDMS), atmospheric DMS surface concentration (DMSSRF), sulfate surface concentration (so4SRF), column-integrated CCN associated with DMS at 0.1% supersaturation (CCNdms) derived from *Vallina et al.* [2007], total column-integrated CCN at 0.1% supersaturation (CCNtot), cloud droplet number concentration at 936 hPa (CDNC), cloud effective radius at 936 hPa (Reff), shortwave cloud forcing (SWCF), aerosol direct effect (ADE) for the IDMS simulation globally, and for the three latitudinal regions. Figure 4b shows all variables have a consistent peak near  $0.25 \text{ yr}^{-1}$  ( $\sim 4 \text{ yr}^{-1}$ ) in the tropical regions ( $30^\circ\text{S}$ – $30^\circ\text{N}$ ). This frequency agrees well with the model simulated ENSO period of roughly  $4 \text{ yr}^{-1}$  that is also evident in the peak frequency of the leading mode EOF PC

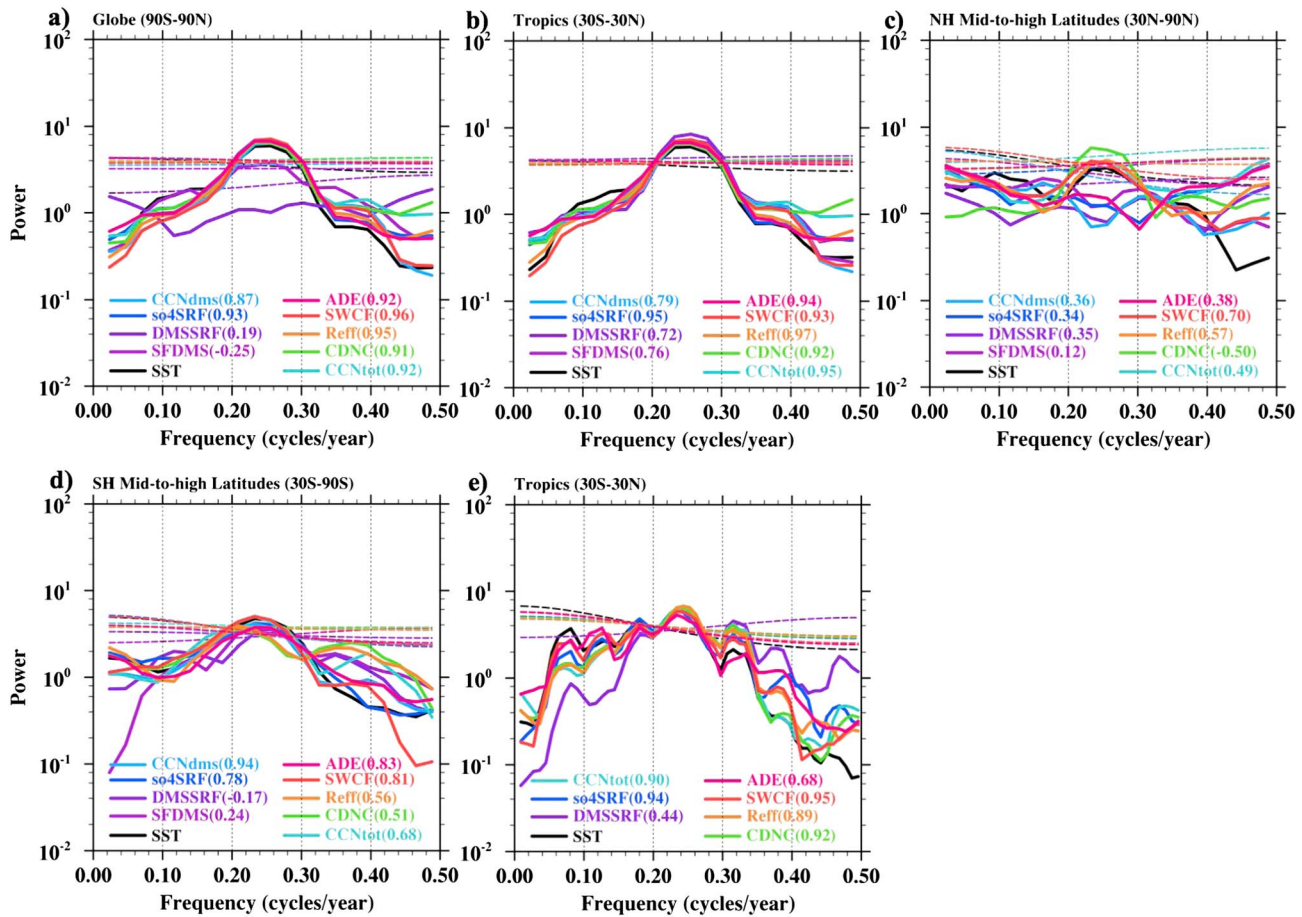


**Figure 4.** The power spectra of the leading mode EOF PC of yearly anomalies of sea surface temperature (SST), DMS emission fluxes (SFDMs), atmospheric DMS surface concentration (DMSSRF), sulfate surface concentration (so4SRF), column-integrated CCN associated with DMS at 0.1% supersaturation (CCNdms) derived from Vallina *et al.* [2007], total column-integrated CCN at 0.1% supersaturation (CCNtot), cloud droplet number concentration at 936 hPa (CDNC), cloud effective radius at 936 hPa (Reff), shortwave cloud forcing (SWCF), aerosol direct effect (ADE) from the IDMS simulation in (a) the globe, (b) the tropics, (c) the Northern Hemisphere middle-to-high latitudes, (d) the Southern Hemisphere middle-to-high latitudes, and from the PDMS simulation in (e) the tropics. The colored dashed lines represent 95% significance levels of corresponding variables. The values inside of the parenthesis represent the correlation coefficient between the leading mode EOF PC of corresponding variables in the legend with that of sea surface temperature yearly anomalies.

of SST anomalies (i.e., black solid line) and is well within the 3–6 year range reported by Deser *et al.* [2012]. This ENSO-like feature is also seen in the global averages of some of the relevant atmospheric properties (Figure 4a); the middle-to-high latitudes in both Northern and Southern Hemispheres (Figures 4c and 4d) show some influence from ENSO teleconnections. However, ENSO-like periodicity does not apply for all variables in these three regions as illustrated by the averages over the tropical region (Figure 4b). In addition, as shown in Figure 2, the IDMS simulation reproduces measured atmospheric DMS surface concentrations in the Pacific Ocean quite well, even though it significantly overestimates concentrations compared to observations over the Southern Ocean. Thus, the following section focuses on results from the tropics (30°S–30°N). The consistent ENSO-like periodicity detected in all properties investigated in Figure 4b suggests that ENSO is the main process that affects the interannual variability of these properties. Moreover, the high-correlation coefficient between the variables investigated and the first-mode EOF PC of SST yearly anomalies ranges from 0.72 (DMS concentrations) up to 0.97 (cloud droplet effective radius), which suggests a close relationship between these variables and SST variations induced by ENSO activities.

We also analyzed the EOFs of these same variables using the PDMS simulation. Figure 4e shows that the power spectra of the leading mode EOF PC of yearly anomalies in the tropical region is similar to that in Figure 4b. All variables show a consistent peak of around  $0.24 \text{ cycles/year}$  ( $\sim 4 \text{ years}$ ) in the tropical regions

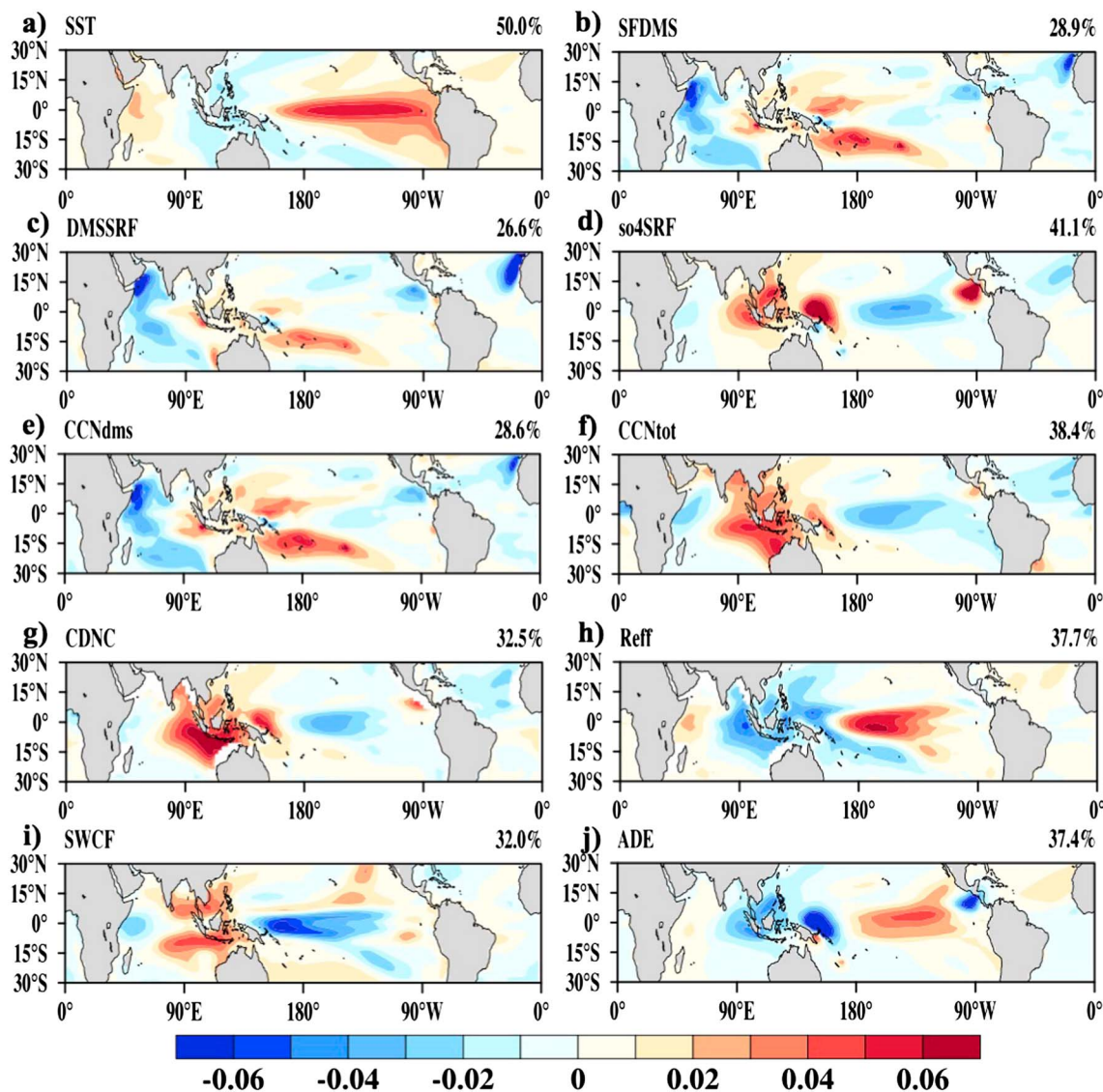


**Figure 5.** The leading mode EOF of yearly anomalies of (a) sea surface temperature (SST), (b) DMS emission fluxes (SFDMS), (c) atmospheric DMS surface concentration (DMSSRF), (d) atmospheric sulfate surface concentration (so4SRF), (e) column-integrated CCN associated with DMS at 0.1% supersaturation (CCNdms) derived using Vallina et al. [2007], (f) column-integrated total CCN at 0.1% supersaturation (CCNtot), (g) cloud droplet number concentration at 936 hPa (CDNC), (h) cloud effective radius at 936 hPa (Reff), (i) shortwave cloud forcing (SWCF), and (j) aerosol direct effect (ADE) from the IDMS simulation. The variance explained by the leading mode EOF is given at the upper right corner of each panel.

( $30^{\circ}\text{S}$ – $30^{\circ}\text{N}$ ), which agrees well with the  $0.25 \text{ cyr}^{-1}$  from the IDMS simulation shown in Figure 4b, but with a power density of 6.1 at the peak that is somewhat lower than the peak power density of 6.9 in the IDMS simulation. The high correlation coefficient found between the variables and the first-mode EOF PC of SST yearly anomalies is comparable to that seen in the IDMS simulation (except DMS surface concentrations). Thus, although the PDMS simulation does not have year-to-year variations of DMS emissions, ENSO still plays an important role in affecting atmospheric DMS abundance by influencing the DMS removal processes and associated aerosol and cloud properties.

Figure 5 shows the leading mode EOF of yearly anomalies for the IDMS simulations of the same variables discussed above. Note we selected the signs of the variables displayed in Figures 5b–5j to make the phasing between variables consistent with the variation of SST in Figure 5a (which is a typical SST pattern during ENSO). The leading EOF mode of DMS flux (Figure 5b) and atmospheric DMS surface concentration (Figure 5c) show 29% and 27% annual variance, respectively. In response to the positive variation in sea

surface temperature extending from the eastern equatorial Pacific Ocean (Figure 5a), the spatial pattern of DMS flux (Figure 5b) and surface air concentration (Figure 5c) show a scissor-like positive pattern over the western Pacific Ocean and a negative counterpart over the eastern Pacific and western Indian Oceans; this contrast between the eastern and western Pacific suggests that the DMS emission flux and atmospheric DMS concentration vary with opposite signs in these two ocean regions. The variation of sulfate aerosols (Figure 5d) that results in part from DMS oxidation shows a similar pattern to that of DMS emission fluxes (Figure 5c) (i.e., displaying the positive and negative pattern over the western and eastern Pacific Ocean, respectively), suggesting a close link between DMS and sulfate aerosols. Sulfate aerosols have a positive pattern over the eastern Pacific Ocean close to the coast of North America, which is in contrast to the negative pattern in DMS emissions and surface concentration; this feature indicates that the variation in sulfate aerosols in these regions may be determined by other processes, such as  $\text{SO}_2$  aqueous-phase oxidation in cloud droplets or  $\text{H}_2\text{SO}_4$  condensation or wet removal by precipitation (shown in Figure S3). The leading EOF mode of sulfate aerosol concentration explains 41% of its annual mean variance. The variation of the DMS-derived CCN (Figure 5e) is in accordance with the DMS surface concentration (Figure 5c), while that of the total CCN (Figure 5f) is consistent with the spatial pattern of sulfate aerosol concentration (Figure 5d).

Cloud droplet number, cloud effective radius, and shortwave cloud forcing (Figures 5g–5i) share major spatial variability in the Pacific Ocean, similar to DMS and sulfate, while the aerosol direct effect (ADE) (Figure 5j) displayed almost the same pattern as the sulfate aerosols (Figure 5d) but is opposite in sign. The leading EOF mode of CCN, cloud droplet number, cloud effective radius, SWCF, and ADE explains 30% to 44% of their corresponding annual variance. Overall, the results of the multivariable EOF analysis show a bipolar feature over the tropical Pacific Ocean, indicating that there may be a relationship between DMS (and related aerosol, cloud, and radiative properties) and ENSO, since they both have similar dominant modes (i.e., first EOF) of interannual variability in the tropical Pacific climate system.

In order to better understand the similarities of the patterns for DMS-related variables (e.g., SFDMS and DMSSRF) and other variables related to sulfate aerosol and cloud microphysical and radiative properties in Figure 5, we investigated the relationship between DMS and sulfate as well as the relationship between sulfate and cloud properties. A close relationship between variations in sulfate aerosol and variations in cloud microphysical and radiative properties is clearly illustrated in Table S1. As shown in Table S2, we calculated the spatial correlation coefficients between the first EOF PC of variables related to sulfate sources and sulfate abundance in the atmosphere in terms of sulfate surface concentration (so4SRF) and sulfate burden (BURDENSO4). The top two aerosol processes that are directly connected to the variability of sulfate loading in the atmosphere over the tropics and that have the highest correlations with sulfate surface concentrations and column-integrated burden are aqueous-phase oxidation of  $\text{SO}_2$  (AQSO2) and  $\text{H}_2\text{SO}_4$  condensation (H2SO4COND), but sulfate wet deposition also shows some correlation. The correlations between DMS-related variables (e.g., SFDMS, DMSSRF, and DMSSO2) and these two processes (i.e., AQSO2 and H2SO4COND) are shown in Table S3. The DMS-oxidation flux to form  $\text{SO}_2$  (DMSSO2) has higher correlations to gas-phase (0.65) and aqueous-phase (0.35) oxidation of  $\text{SO}_2$  (to form sulfuric acid gas and sulfate) than to DMS emissions or its surface concentrations, suggesting that the internal variability of oxidants (i.e., OH) also plays some role in contributing to variations in sulfate. Note that sulfur emissions originating from volcanic eruptions prescribed at the year 1850 [Dentener et al., 2006] do not have year-to-year variations like DMS emissions. This means that year-to-year variations in DMS emissions are the only source that affects the variations in sulfate, making the variability of DMS emissions of great importance for causing changes in sulfate aerosol concentrations and its associated cloud microphysical and radiative properties.

We further calculated composites of monthly anomalies for the top 10% warmest and coldest ENSO events during the 140 year simulation, following the first-mode EOF PC of monthly SST anomalies in the tropical regions ( $30^{\circ}\text{S}$ – $30^{\circ}\text{N}$ ). The warm ENSO phase (El Niño) is characterized by warm sea surface temperature anomalies over the eastern Pacific Ocean and dry conditions over Indonesia, while the cold ENSO phase (La Niña) displays the opposite pattern. Cold temperatures favor phytoplankton blooms that are proxies for upwelling and associated nutrient supply [Chavez et al., 1998, 1999; Leonard and McClain, 1996]. The simulated mean aerosol properties including sulfate burden, aerosol number concentration, aerosol optical depth,

**Table 2.** Climatological Monthly Mean Sulfate Burden (BURDENSO4), Accumulation Mode Aerosol Number Concentration at Surface (AERNUM), Aerosol Optical Depth (AOD), and Cloud Condensation Nuclei at 0.1% Supersaturation at Surface (CCN) Averaged Over Oceans in the Tropics (30°S–30°N)

	Mean	Reference <sup>a</sup>
BURDENSU ( $\text{mg m}^{-2}$ )	1.1	<8
AERNUM ( $\text{cm}^{-3}$ )	135.6	<500
AOD	0.1	<0.8
CCN ( $\text{cm}^{-3}$ )	70.7	<250

<sup>a</sup>Liu et al. [2012].

and CCN averaged over oceans in the tropics (30°S–30°N) fall within the range of values simulated by the previous study [e.g., Liu et al., 2012], as summarized in Table 2. Figure 6 shows the composite differences of monthly anomalies of relevant variables between average values during cold and warm events (i.e., cold-warm). The DMS flux (Figure 6a) and DMS surface concentration (Figure 6b) in the cold phase increase in the eastern Pacific Ocean and decrease in Indonesia,

in response to changes in sea water concentrations of DMS (Figure 6l), diatom sulfur (Figure 6m), chlorophyll (Figure 6n), and wind speed (not shown here). The change in DMS fluxes leads to similar changes in sulfate aerosol surface concentration (Figure 6c) and aerosol optical depth (Figure 6d), which then results in strong cooling of the eastern and central Pacific and warming in the western Pacific (Figure 6h) through direct scattering of solar radiation by the aerosol (AKA aerosol direct effect). Note that the decrease in sulfate aerosol concentration (Figure 6c) in the eastern Tropical Pacific close to the coasts of Mexico and Ecuador results from an increase in wet deposition (not shown here). The variation in sulfate aerosol concentration (Figure 6c) that originates from DMS oxidation contributes to the corresponding increase of cloud condensation nuclei (Figure 6e) and cloud droplet number at 936 hPa (Figure 6f) over the eastern Pacific Ocean. The largest absolute difference in Aerosol Optical Depth (AOD) between El Niño and La Niña events is about  $\pm 0.05$  (Figure 6d), suggesting that the relative difference could be up to 50% given the mean AOD of 0.1 in the tropical Pacific (Table 2). This large relative difference in AOD is partially due to the opposite signs of the AOD anomalies in the warm and cold phases in the same regions. These anomalies can be attributed to both sea-salt aerosol and DMS-related sulfate aerosol as quantified below.

Changes in the variables (e.g., AOD, CCN, CDNC, Reff, ADE, and SWCF) over the tropics discussed in Figure 6 may be attributed to variations in DMS-derived sulfate, volcanic sulfate, and sea salt. As described in section 2, sulfur emissions originating from volcanic eruptions prescribed at the year 1850 are mainly located over continents and islands [Dentener et al., 2006] and do not have year-to-year variations like the DMS emissions. Additionally, the SO<sub>2</sub> released from volcanic eruptions mainly located in the upper troposphere and lower stratosphere may limit their influence on CCN at the marine boundary layer. Although the model does not separately track sulfate aerosols formed from volcanic sulfur emissions and DMS oxidation, variations in sulfate aerosols result from two types of processes: the first is changes in DMS emissions and the second is process-based variations (e.g., dry or wet deposition and gas- or aqueous-phase oxidation). To compare the contributions from sulfate and sea salt to the interannual aerosol variations, we calculated spatial correlation coefficients between sulfate and sea-salt burden in Table 3. Sea-salt and sulfate burdens contribute roughly 79% and 28% of the variance in AOD (i.e., the square of correlation coefficients) to the composite differences between warm and cold ENSO phases over the tropics, respectively, suggesting that sea salt plays a more important role than sulfate in controlling the variations in AOD between the warm and cold ENSO phases. However, due in part to the higher scattering by sulfate particles in the accumulation mode, sulfate aerosol (roughly 85%) has a larger contribution to changes in direct effects between cold and warm ENSO than sea salt (roughly 8%). Moreover, because sulfate aerosol dominates both aerosol mass and number in the accumulation mode, sulfate aerosol contributes 54% more to the spatial variation of CCN and, subsequently, of CDNC and Reff between warm and cold phases of ENSO. Hence, sulfate (16%) has a higher contribution to changes in SWCF over the tropics than sea salt (1%) between cold and warm phases of ENSO. If the liquid water path is constant and the cloud droplet number is increased over the eastern Pacific Ocean, we expect smaller droplets and larger droplet surface area and hence greater cloud reflectivity [Twomey, 1974]. This would lead to a stronger aerosol first indirect effect at the top of the atmosphere, which would cause surface cooling. Simultaneously, smaller cloud droplets induced by an increase of sulfate aerosol would enhance the aerosol second indirect effect by decreasing precipitation efficiency and thereby prolonging cloud lifetime and increasing cloud liquid water path, which further limits sunlight from reaching the surface [Albrecht, 1989]. Thus, starting from increased DMS emission fluxes caused by stronger upwelling associated

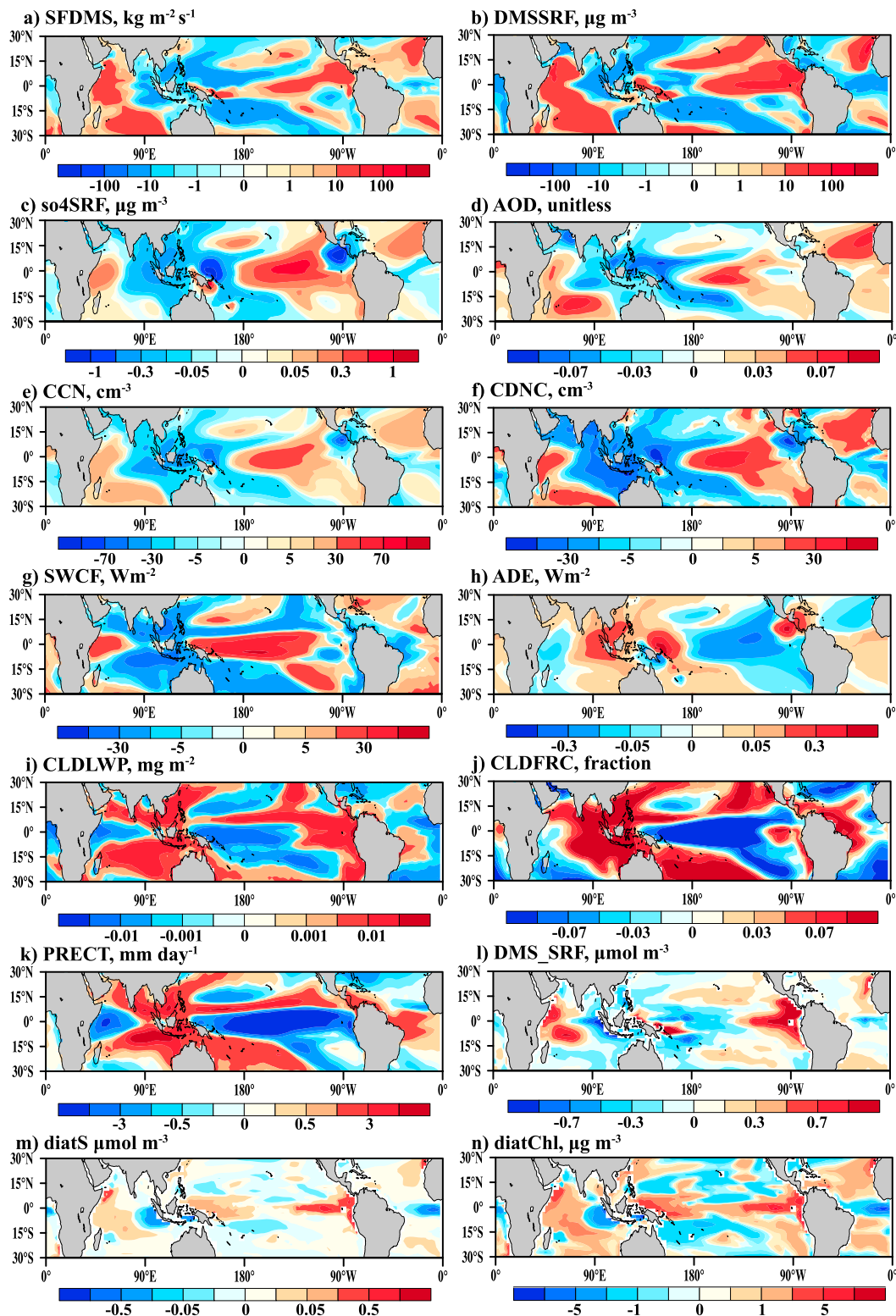


**Figure 6.** Composite difference between the top 10% warm and cold phase of ENSO events in monthly anomalies of the IDMS simulation for (a) DMS emission fluxes ( $\text{SFDMs, kg m}^{-2} \text{ s}^{-1}$ ), (b) atmospheric DMS surface concentration ( $\text{DMSSRF, } \mu\text{g m}^{-3}$ ), (c) sulfate surface concentration ( $\text{so4SRF, } \mu\text{g m}^{-3}$ ), (d) aerosol optical depth (AOD, unitless), (e) CCN at 0.1% supersaturation at 936 hPa ( $\text{CCN, cm}^{-3}$ ), (f) cloud droplet number concentration at 936 hPa ( $\text{CDNC, cm}^{-3}$ ), (g) shortwave cloud forcing (SWCF,  $\text{W m}^{-2}$ ), (h) aerosol direct effect (ADE,  $\text{W m}^{-2}$ ), (i) cloud liquid water path (CLDLWP,  $\text{mg m}^{-2}$ ), (j) cloud fraction (CLDFRC, fraction), (k) precipitation (PRECT,  $\text{mm d}^{-1}$ ), (l) seawater DMS concentration (DMS\_SRF,  $\mu\text{mol m}^{-3} \text{ s}^{-1}$ ), (m) sea surface diatom sulfur concentration (diatS,  $\mu\text{mol m}^{-3} \text{ s}^{-1}$ ), and (n) sea surface diatom chlorophyll concentration (diatChl,  $\mu\text{g m}^{-3}$ ).

**Table 3.** Spatial Correlation Coefficients Between Sulfate Burden (BURDENSO4) and Sea-Salt Burden (BURDENSS) and Aerosol Optical Depth (AOD), CCN at 0.1% Supersaturation at 936 hPa (CCN), Cloud Droplet Number Concentration at 936 hPa (CDNC), Cloud Droplet Effective Radius at 936 hPa (Reff), Aerosol Direct Effect (ADE), and Shortwave Cloud Forcing (SWCF), Respectively, for Composite Difference Between the Top 10% Warm and Cold Phase of ENSO Events in Monthly Anomalies of the IDMS Simulation

	BURDENSO4	BURDENSS
AOD	0.53	0.89
CCN	0.82	0.28
CDNC	0.77	0.21
Reff	-0.78	-0.41
ADE	-0.92	-0.29
SWCF	0.40	0.10

the decrease of SWCF spanned the entire equatorial Pacific (i.e., shaded red area between 15°S and 15°N), partly resulting from the decrease of the cloud liquid water path (Figure 6i) and cloud fraction (Figure 6j) induced by colder sea surface temperatures. Negative anomalies of SWCF and ADE (i.e., blue colors) represent stronger cooling than normal and vice versa. Figure 6k shows the change of precipitation corresponding to the increase in cloud droplet number concentration and the decrease in cloud fraction. In summary, during cold ENSO episodes, sulfate aerosols associated with DMS contributed to strengthening the aerosol direct effect and the first aerosol indirect effect while damping the second indirect effect. The damped second aerosol indirect effect results from competition with changes in cloud liquid water path and cloud fraction caused by variations in sea surface temperatures. Aerosols that dampen cloud shortwave radiative effects are also described by Yang *et al.* [2016].

The DMS-sulfate-cloud relationship is also evident in satellite-observed relevant variables, including chlorophyll concentration, 10 m wind speed, fine-particle aerosol optical depth, cloud top droplet number concentration, cloud liquid water path, cloud fraction, shortwave cloud radiative effect, and precipitation. In Figure 7, the differences between the observed values of these relevant variables for the top 10% coldest and warmest ENSO events are comparable to those shown in Figure 6. Cold and warm ENSO events were sorted using the Niño3.4 index provided by the National Oceanic and Atmospheric Administration (NOAA) (<http://www.cpc.ncep.noaa.gov/data/indices/ersst4.nino.mth.81-10.ascii>). Compared to those in El Niño events, the observed seawater chlorophyll concentration during La Niña events increases over the eastern Pacific Ocean (Figure 7a), which suggests a greater phytoplankton bloom. The large phytoplankton bloom shown in seaWiFS chlorophyll observations over the equatorial Pacific that followed recovery from the 1997–1998 El Niño and during the subsequent La Niña period was reported in previous studies [Chavez *et al.*, 1999; Behrenfeld *et al.*, 2001]. The spatial correlation coefficient between modeled seawater chlorophyll concentration and surface seawater DMS concentration is about 0.6 in the Niño 3 region (150°W–90°W, 5°S–5°N) over the eastern Pacific Ocean, suggesting that chlorophyll might be a good proxy for DMS ventilated into the atmosphere in this region. Additionally, the 10 m wind speed from the National Centers for Environmental Prediction (NCEP) reanalysis data increases over the eastern equatorial Pacific Ocean (Figure 7b). DMS emissions into the atmosphere should be expected to show corresponding increases in the same region due to the wind-induced increases in sea-air transfer. Figure 7c shows that fine-particle aerosol optical depth increases over the eastern Pacific Ocean during La Niña, causing a resulting increase in cloud droplet number concentration (Figure 7d) [Quaas *et al.*, 2006] over the northeastern Pacific Ocean. The response of observed shortwave cloud radiative effects derived from the Clouds and the Earth's Radiant Energy System (CERES) satellite (Figure 7g) shows variation across the equatorial Pacific Ocean that is similar to the modeled SWCF response (Figure 6g), which results partly from altering the cloud liquid water path (Figure 7e) and cloud fraction (Figure 7f) between the cold and warm ENSO phases. On the other hand, in response to increases in cloud droplet number concentration and the decrease in cloud fraction over the northeastern Pacific and central equatorial Pacific Oceans, the Global Precipitation Climatology Project (GPCP) precipitation (Figure 7h) decreases over the same region. Aerosol and cloud properties illustrated in Figure 7 include a large portion of aerosols of anthropogenic origin and, thus, showed some expected discrepancies between

with lower sea surface temperature during La Niña events and ending with surface cooling, the simulated DMS-sulfate-cloud relationship produces a positive feedback on interannual timescales that is consistent with the first half of the feedback loop of Charlson *et al.* [1987]. However, in the simulation, the effects of the hypothetical aerosol cooling on shortwave cloud radiation may be counteracted by other dynamic influences during La Niña episodes (e.g., reducing SWCF either by the decrease of cloud fraction or smaller cloud liquid water path). In Figure 6g,

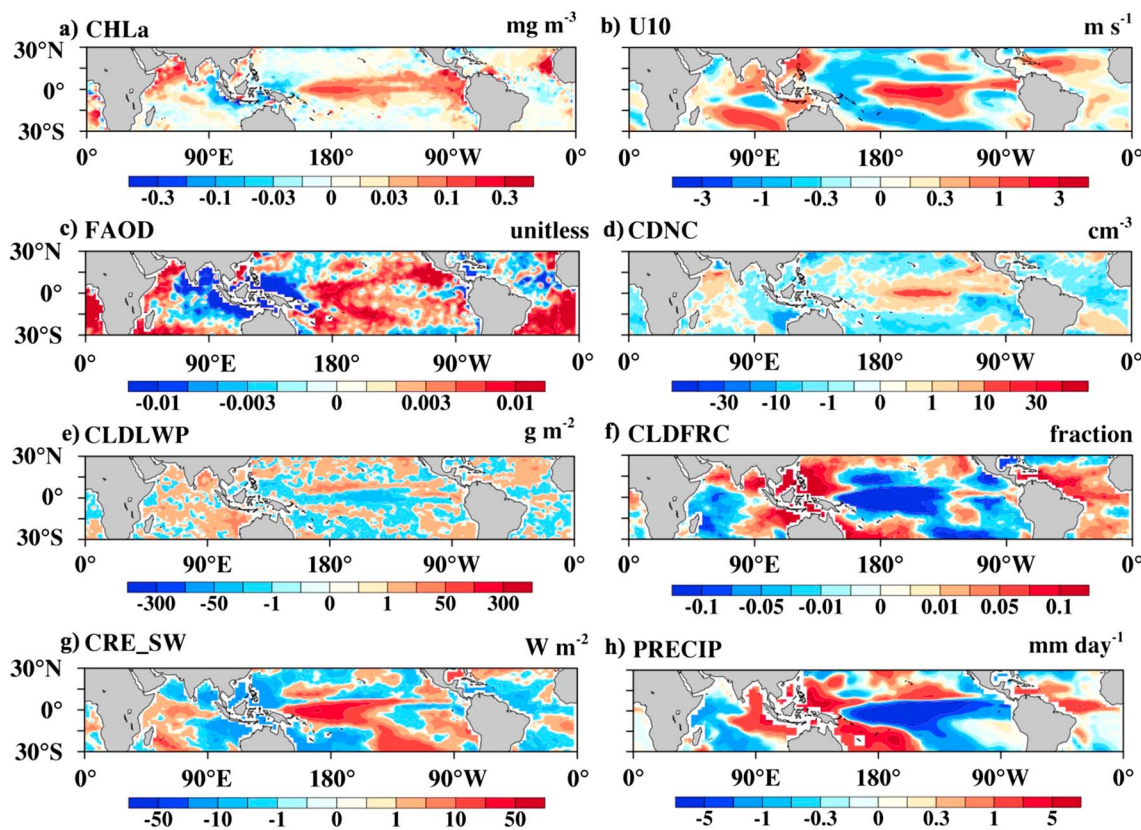


**Figure 7.** Composite difference between the top 10% cold and warm phase of ENSO events (i.e., cold-warm) in monthly anomalies of (a) SeaWiFS chlorophyll concentration (CHLa,  $\text{mg m}^{-3}$ ) during 1997–2010, (b) NCEP 10 m wind speed ( $\text{U10, m s}^{-1}$ ) during 1948–2014, (c) fine-particle aerosol optical depth (FAOD, unitless), (d) cloud top droplet number concentration (CDNC,  $\text{cm}^{-3}$ ) derived from Quaas et al. [2006], (e) cloud liquid water path (CLDLWP,  $\text{g m}^{-2}$ ) and (f) cloud fraction (CLDFRC, fraction) from the Moderate Resolution Imaging Spectroradiometer during 2000–2015, (g) shortwave cloud radiative effect (CRE\_SW,  $\text{W m}^{-2}$ ) from the CERES during 2000–2014, and (h) precipitation ( $\text{mm d}^{-1}$ ) from the GPCP during 1979–2015.

the present-day observations and the preindustrial model simulations in terms of the composite difference between cold and warm ENSO events. As discussed in Figure 6, changes in fine AOD, CDNC, and CRE\_SW in Figure 7 over the tropics can be attributed to variations in both DMS and sea salt; however, sulfate provides the majority of the aerosol mass and number in the accumulation mode, making its contribution to affecting cloud microphysical properties (e.g., CDNC) and subsequent cloud radiative effect likely to be substantial. Based on similarities in modeled (Figure 6) and observed (Figure 7) composite difference from variables connected with the aerosol-cloud interaction between cold and warm ENSO events, we suggest that DMS and its associated sulfate aerosol, cloud, and radiative properties exhibit a distinct behavioral response to changes in atmospheric properties between these two ENSO phases.

The association between sea-to-air DMS emission flux and ENSO could arise through changes in sea-to-air transfer rate (primarily mediated by 10 m wind speed), DMS seawater concentration, or both. Changes in DMS seawater concentration associated with ENSO may be influenced by upwelling (which brings nutrient-rich deep water to the surface to stimulate phytoplankton photosynthesis, hence producing more DMS) in the model. Figure 8 shows the regression coefficient between the model's ENSO index (i.e., the first-mode EOF PC of sea surface temperature yearly standardized anomalies between  $30^{\circ}\text{S}$  and  $30^{\circ}\text{N}$ ) and (a) sea-to-air DMS emission flux, (b) seawater DMS surface concentration, (c) 10 m wind speed, and (d) vertical velocity near the oceanic depth of 100 m. Note that we used vertical velocity at the oceanic depth of 100 m as a proxy of local upwelling in the shallow ocean regime. The temporal variability in sea-to-air DMS emission flux is most similar to variability in 10 m wind speed (Figure 8c versus Figure 8a). Spatial correlation coefficients between the regression of ENSO on DMS flux (Figure 8a) and the regressions of ENSO on seawater DMS, 10 m wind speed, and ocean vertical velocity (Figures 8b–8d) in latitude

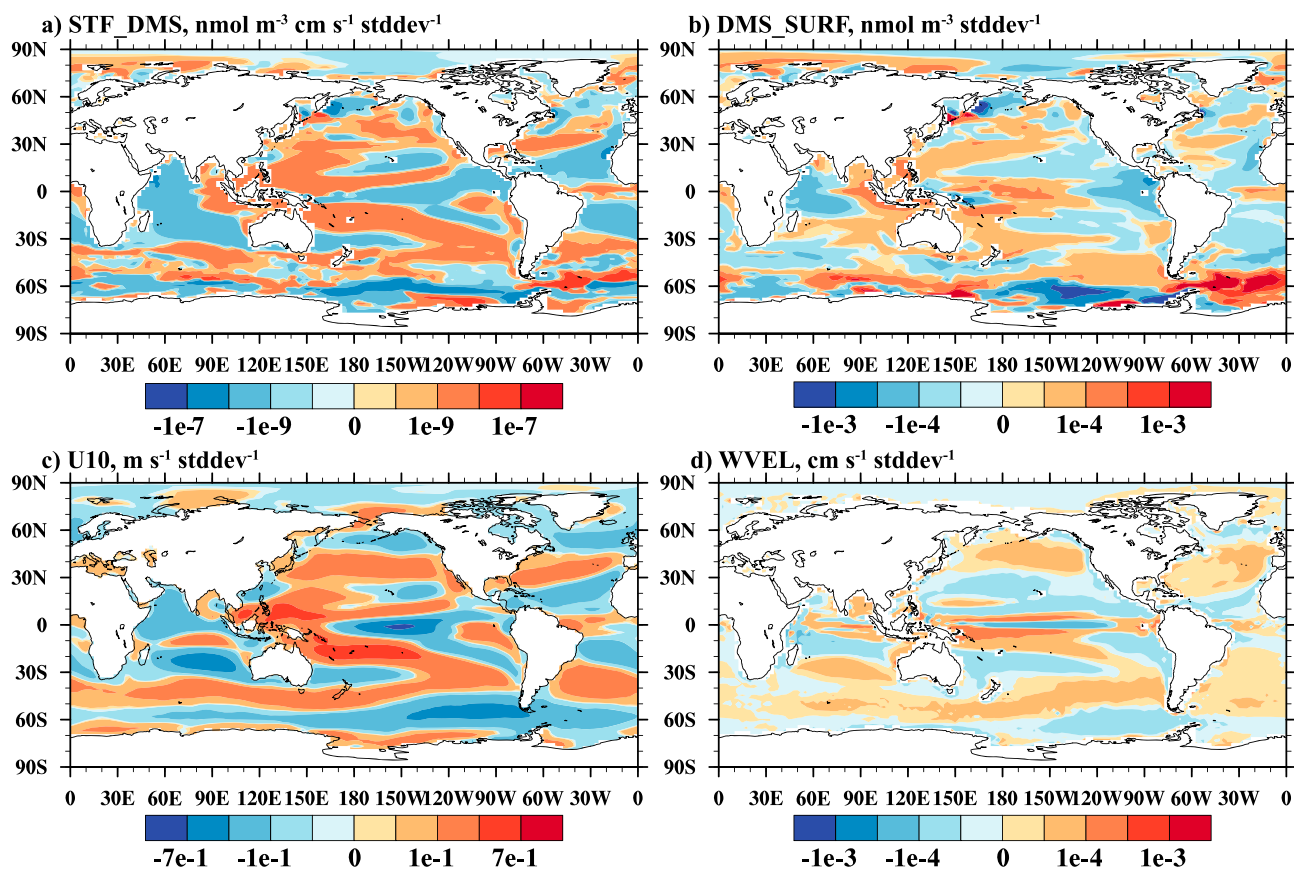


**Figure 8.** Regression coefficient between the model's ENSO index and (a) sea-to-air DMS emission flux (STF\_DMS), (b) sea water DMS surface concentration (DMS\_SURF), (c) 10 m wind speed, and (d) vertical velocity near the depth of 100 m.

bands of 30°S–30°N over ocean are 0.55, 0.75, and 0.13, respectively. This difference in spatial correlation coefficients suggests that wind speed change is the largest driver of the association between ENSO and DMS emission flux ventilated into the atmosphere within the tropics. The effects from changes in DMS seawater concentration with ENSO are also evident. For example, the negative response to ENSO off the east coast of South America along the equatorial Pacific Ocean (Figure 8b) and over the Indian Ocean may counteract the positive response ascribed to the 10 m wind in the same region (i.e., orange shaded area off the west coast of South America and in the Indian Ocean in Figure 8c). The vertical velocity (Figure 8d) has a relatively small direct influence on sea-to-air DMS emissions, although the change in upwelling of the upper ocean typically accompanies the variation in sea surface winds. This comparison indicates that the DMS emission flux into the atmosphere is stronger during the cold phase of ENSO, primarily due to increased surface winds causing greater sea-air transfer, with some contribution from the higher DMS concentration in surface waters.

We investigated interannual variability using in situ point measurements of non-sea-salt sulfate (i.e., nss-sulfate) mass concentration produced during the early 1980s to the late 1990s by the Global Aerosol Climatology Project ([http://gacp.giss.nasa.gov/data\\_sets/Joseph\\_Prospéro.html](http://gacp.giss.nasa.gov/data_sets/Joseph_Prospéro.html)). We used measurements that were categorized as “high-quality” from five stations located in the Pacific Basin (Cape Grim, 1983–1996; Fanning Island, 1981–1986; Midway Island, 1981–2000; Oahu, 1981–1995; and American Samoa, 1983–1999), as recommended by Spada *et al.* [2013]. The measurements were binned into monthly averages, and then temporal anomalies were computed following Xu *et al.* [2015]. Here the modern sulfate observations are used in order to support, to the limited extent possible, the validity of the preindustrial predictions of variability in DMS and non-sea-salt sulfate. In Figure 9, the first five panels show a correlation between nss-sulfate mass concentration anomalies and the observed global sea surface temperature anomalies. Here we focus our investigation and discussion on the local

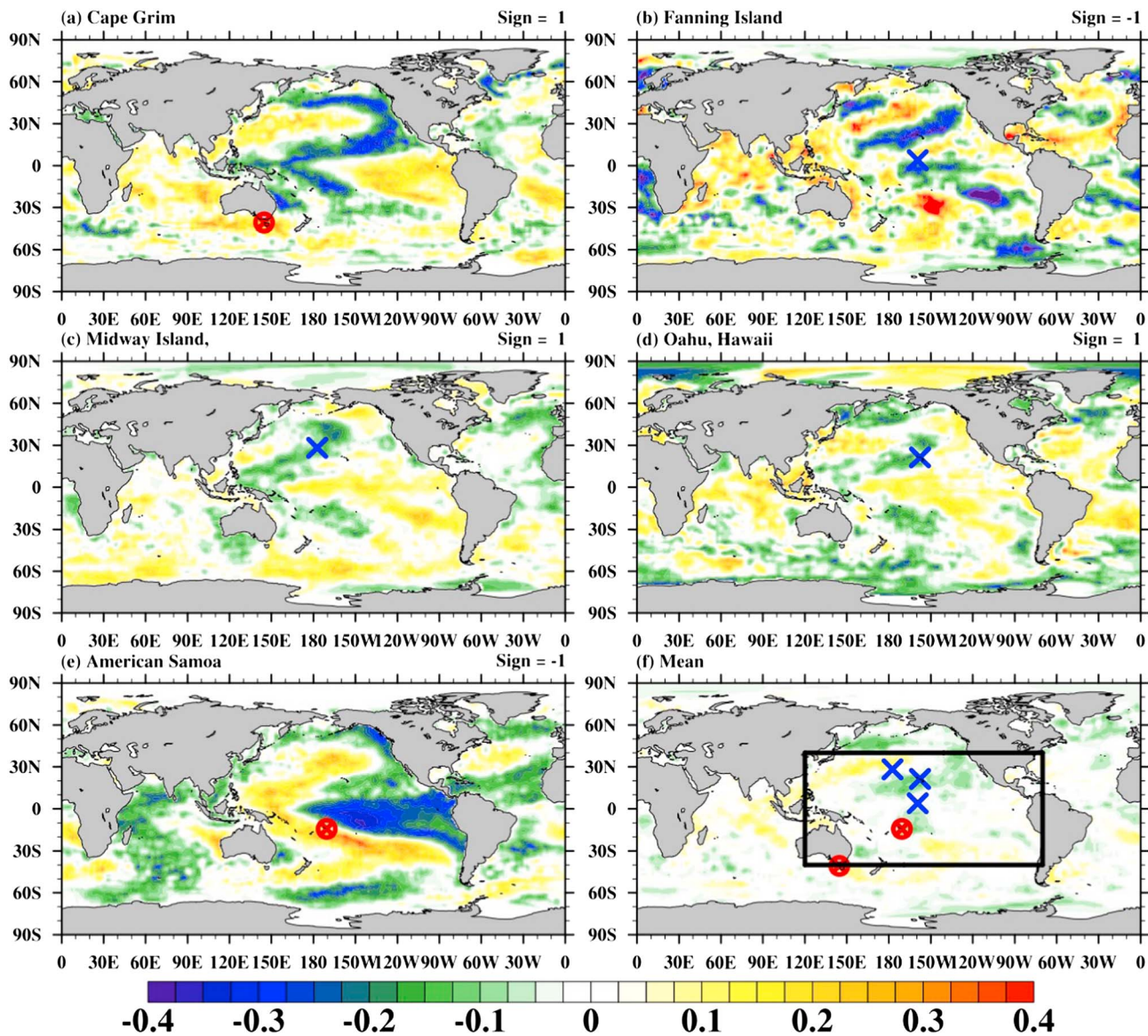


**Figure 9.** The correlation between the in situ monthly non-sea-salt sulfate mass concentration anomalies measured at (a–e) five stations (as indicated in the panel titles) and observed monthly sea surface temperature anomalies, and their (f) mean response. Cape Grim and American Samoa are marked as red circles, while Fanning Island, Midway Island, and Oahu are marked as blue crosses. The black rectangular box ( $40^{\circ}\text{S}$ – $40^{\circ}\text{N}$ ;  $120^{\circ}\text{E}$ – $70^{\circ}\text{W}$ ) marked in Figure 9f is the tropic Pacific basin in which our discussion is focused on.

aerosol-ENSO interaction in the tropical Pacific basin (i.e.,  $40^{\circ}\text{S}$ – $40^{\circ}\text{N}$ ;  $120^{\circ}\text{E}$ – $70^{\circ}\text{W}$ ) marked in Figure 9f because in situ aerosol measurement stations selected in this region are located in the clean marine environment comparable to preindustrial conditions. Each station shows a hemispherically symmetric relationship that is similar in spatial pattern to ENSO. A negative relationship between sulfate aerosol and tropical Pacific SST is evident at Fanning Island and American Samoa, given the negative sign shown in the upper right corner of each panel, while a positive relationship is seen at the other three stations. We took the appropriate signs into account and then averaged correlations at all stations to reduce the influence from noise and local effects. The resulting mean correlation between nss-sulfate and sea surface temperature anomalies shows a positive value over the western Pacific Ocean and a negative value over the eastern equatorial Pacific Ocean, indicating that the observed variability of DMS-associated sulfate aerosols has ENSO-like fluctuations in the Pacific Ocean. In other words, ENSO events reduce DMS fluxes and subsequently DMS-derived sulfate aerosols over the eastern equatorial

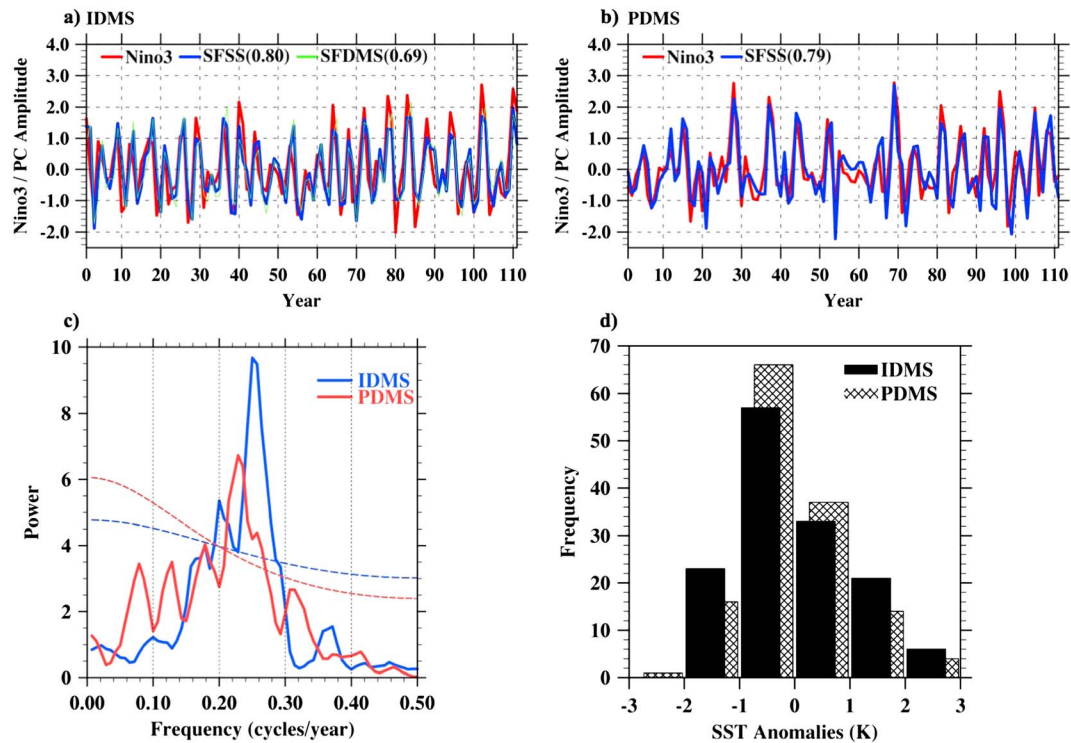


**Figure 10.** Time series of Niño 3 and the first EOF PC of sea-salt (i.e., SFSS) and DMS emissions (i.e., SFDMS) in the tropics ( $30^{\circ}\text{S}$ – $30^{\circ}\text{N}$ ) from (a) IDMS and (b) PDMS simulations during the year of 40–150 and (c) the power spectra and (d) histogram of yearly anomalies of sea surface temperature (K) in the Niño 3 region ( $5^{\circ}\text{S}$ – $5^{\circ}\text{N}$ ;  $150^{\circ}\text{W}$ – $90^{\circ}\text{W}$ ) from the 140 year simulation with interactively calculated DMS emission (IDMS) and the 140 year simulation with prescribed DMS emission (PDMS). The values in parentheses in Figures 10a and 10b represent correlation coefficients between Niño 3 and the first EOF PC of sea-salt and DMS emissions. The dashed lines in Figure 10c represent 95% significance levels.

Pacific Ocean. The negative response of nss-sulfate to changes in sea surface temperature over the eastern Pacific Ocean may be caused by colder temperature producing higher phytoplankton productivity and more sea-to-air DMS emission flux over the eastern Pacific Ocean (Figure 6a). It may also result from increased condensation sinks (e.g., increases in sea-salt surface area due to high winds) or enhanced oxidant loadings in the troposphere (e.g., increases in ozone concentrations due to suppressed convection) over the eastern Pacific Ocean during La Niña conditions.

The simulation with the prescribed monthly DMS emission flux (i.e., PDMS) that uses the climatology developed by *Kettle and Andreae [2000]* provides further understanding of the differences between atmospheric DMS concentrations, as well as associated aerosols, and the cloud and radiative properties that result from those DMS emission variations. As reported in recent studies, phytoplankton blooms may strengthen [*Lengaigne et al., 2007; Anderson et al., 2007; Marzeion et al., 2005; Ballabrera-Poy et al., 2007; Löptien et al., 2009*] and weaken [*Jochum et al., 2010; Wetzel et al., 2006; Timmermann and Jin, 2002; Zhang et al., 2009*] ENSO variability by altering light absorption and, thus, changing the vertical heat distribution in the upper ocean [*Lewis et al., 1990*]. Over the tropical oceans, we acknowledge that the variability of sea-salt emission exerts a feedback on the climate through the aerosol-cloud-radiation interaction in addition to the role of DMS. We show time series of the yearly Niño 3 index and the first EOF PC of yearly sea-salt (i.e., SFSS) and DMS emissions (i.e., SFDMS) in the tropics ( $30^{\circ}\text{S}$ – $30^{\circ}\text{N}$ ) from IDMS and PDMS simulations during years 40–150 in Figures 10a and 10b. The subset of the 111 year period is chosen here because the IDMS model included sea-salt emissions starting from the year 40. The first EOF PC of sea-salt and DMS emissions correlates strongly with the Niño 3 index in both IDMS and PDMS simulations, suggesting that the variability of both sea salt and DMS has a close relationship with variations in sea surface temperature in the Niño 3 region ( $5^{\circ}\text{S}$ – $5^{\circ}\text{N}$ ;  $150^{\circ}\text{W}$ – $90^{\circ}\text{W}$ ). We conduct

linear regressions using the first EOF PC of yearly sea-salt and/or DMS emission as predictors in the IDMS simulation and only sea-salt emission in the PDMS simulation as follows:

$$\text{Nino3}_{\text{IDMS}, 1} = \beta_1 \text{SFSS}_{\text{IDMS}} + \beta_2 \text{SFDMS}_{\text{IDMS}} + \varepsilon \quad (1)$$

$$\text{Nino3}_{\text{IDMS}, 2} = \beta_1 \text{SFSS}_{\text{IDMS}} + \varepsilon \quad (2)$$

$$\text{Nino3}_{\text{PDMS}} = \beta_1 \text{SFSS}_{\text{PDMS}} + \varepsilon \quad (3)$$

where  $\text{Nino3}_{\text{IDMS}, 1}$  (or  $\text{Nino3}_{\text{IDMS}, 2}$ ),  $\text{Nino3}_{\text{PDMS}}$ ,  $\text{SFSS}_{\text{IDMS}}$ ,  $\text{SFSS}_{\text{PDMS}}$ , and  $\text{SFDMS}_{\text{IDMS}}$  are yearly Niño 3 and the first EOF PC of yearly sea salt (i.e., SFSS) and DMS emissions (i.e., SFDMS) in the tropics ( $30^{\circ}\text{S}$ – $30^{\circ}\text{N}$ ) from IDMS and PDMS simulations during the years of 40–150, respectively, and  $\varepsilon$  is an error term. The first regression (i.e., equation (1)) including both sea salt and DMS emissions as explanatory variables accounts for approximately 69% of the Niño 3 variance (according to the coefficient of determination  $R^2$  of the regression fit for equation (1) is 0.69) in the IDMS simulation. If excluding DMS emission variability in the IDMS simulation, the second regression (i.e., equation (2)) explains roughly 63% of the Niño 3 variance, similar to 62% in the regression applied for the PDMS simulation (i.e., equation (3)). The discrepancy in the regression fit between IDMS and PDMS simulations shed light on the important role of the variability of DMS emission in contributing to year-to-year variations in sea surface temperature anomalies in the Niño 3 region.

Figures 10c and 10d show the power spectra and histogram of yearly anomalies of SST in the Niño 3 region ( $5^{\circ}\text{S}$ – $5^{\circ}\text{N}$ ;  $150^{\circ}\text{W}$ – $90^{\circ}\text{W}$ ) for the 140 year IDMS and PDMS simulations. Both simulations show a statistically significant peak around  $0.23$ – $0.25 \text{ c yr}^{-1}$  (Figures 4b and 4e). However, the spectrum from the IDMS simulation has more power near the peak than in the PDMS simulation, which also has some statistically insignificant fluctuations at lower frequencies. In Figure 10b, Niño 3 SST anomalies from the PDMS simulation are skewed to the right (0.88) more than the 0.49 skewness in the IDMS simulation; the much higher skewness of the PDMS simulation indicates that El Niño events in the PDMS simulation had higher amplitudes than IDMS. In addition, this difference in the skewness between the IDMS and PDMS simulations suggests that allowing DMS emission fluxes to vary (with SST and surface winds) increases the frequency of La Niña events. Standard deviations of Niño 3 SST anomalies from both IDMS and PDMS simulations were  $1^{\circ}\text{C}$ , indicating that the year-to-year changes in DMS emissions in the IDMS simulation do not contribute to altering the modeled ENSO variability in terms of the amount of variations in Niño 3 SST anomalies.

#### 4. Discussion and Conclusions

We investigated the variability of DMS and sulfate aerosol particles (the oxidized product) emitted from the ocean, along with their influence on cloud and radiative properties. We employed a 150 year simulation under preindustrial conditions using the Community Earth System Model embedded with a dynamic DMS module. The model developed here simulates a spatial distribution for DMS emissions and abundance in the atmosphere that is similar to observations [Kettle and Andreae, 2000; Boucher *et al.*, 2003; Kloster *et al.*, 2006]. The model simulates high DMS fluxes over regions with high persistent wind speed (including the broad latitudinal band between  $40^{\circ}\text{S}$  and  $60^{\circ}\text{S}$  over the Southern Ocean and storm track regions over the North Pacific Ocean) and over regions of the equatorial Pacific and Atlantic Oceans where sea surface DMS concentrations are high. The model reproduced observed atmospheric DMS surface air concentrations in the Pacific Ocean within a factor of 2 but simulated excessively high DMS fluxes and subsequent atmospheric DMS burden over the Southern Ocean and the Arctic region. These large biases may be primarily attributed to the simple treatment of one sulfate-rich phytoplankton, *Phaeocystis* [Elliott, 2009]; however, this phytoplankton type is not very important in the tropics, which is the focus of our analyses. The sulfur budget associated with DMS,  $\text{SO}_2$ ,  $\text{H}_2\text{SO}_4$ , and sulfate aerosol sources, sinks, burden, and lifetime is comparable to previous studies [Kloster *et al.*, 2006; Textor *et al.*, 2006; Liu *et al.*, 2012].

The model results show that on interannual time scales, tropical DMS, and related sulfate aerosols, clouds, and radiative properties primarily respond to ENSO cycle, displaying an ENSO-like spatial pattern of coherent variability in the tropical Pacific. The variation in DMS emissions and burden, as well as relevant sulfate and cloud variables (in terms of the first-mode EOF PC) significantly correlate with variations in sea surface temperature in the tropics (Figure 4). The relationship between ENSO and sea-to-air DMS emission fluxes arises primarily from the influence of ENSO on wind speed. ENSO-related changes in ocean surface

temperatures and ocean surface DMS concentrations also contributed but caused only small fractions of the variability.

In order to compare our model simulations with observations, we computed the difference between cold and warm ENSO composites from modeled variables connected to the DMS-sulfate-cloud interaction in the tropical region, which show clear ENSO-like features over both the eastern and western tropical Pacific Oceans. We also found a strong positive forcing by a modulation of ENSO on the DMS-sulfate-cloud interaction during cold ENSO episodes, in accordance with the DMS-aerosol part of the loop of the CLAW hypothesis [Charlson *et al.*, 1987] on interannual timescales. A similar spatial pattern, in terms of the difference in the composites of aerosol and cloud properties between the cold and warm ENSO, was also found from satellite observations. The mean negative (and positive) correlation between in situ measured non-sea-salt sulfate mass concentration anomalies and observed sea surface temperature anomalies in the eastern (and western) Pacific provided observational evidence that colder temperatures accompany higher phytoplankton productivity and, hence, larger DMS fluxes ventilated into the atmosphere. This suggests that DMS, as well as associated aerosols and cloud and radiative properties, exhibits distinct behavior in response to changes in atmospheric properties associated with ENSO.

To understand atmospheric DMS concentration and its associated aerosols and cloud and radiative properties in relation to variation in DMS emissions, we conducted an alternative simulation with prescribed climatological monthly DMS emissions. We found that ENSO affects atmospheric DMS abundance through its influence on the DMS removal process and its associated aerosols and cloud properties, although the year-to-year variability of DMS emission flux is excluded from the prescribed DMS simulation. On the other hand, while the variability of both DMS and sea salt emissions could play important roles in exerting a feedback on the climate through the aerosol-cloud-radiation interaction, including the variation of the DMS emission flux increased the frequency of La Niña events but may not contribute to altering the magnitude of ENSO variability in terms of the standard deviation of Niño 3 SST anomalies. Thus, there seems to be a two-way interaction between DMS and ENSO (via aerosols, clouds, and their radiative properties) in the tropical region. Additional efforts are needed to further explore how changes in the radiation induced by DMS-associated aerosols and clouds exert a feedback on oceanic DMS production.

Sulfate aerosols originating from oceanic DMS emissions constitute a significant source of natural aerosols, and natural aerosol concentrations have higher uncertainties [Carslaw *et al.*, 2013] compared to those of anthropogenic origin. Consequently, our results suggesting a positive feedback between DMS and enhanced cloud induced cooling may provide insights into understanding the CLAW hypothesis on interannual timescales. Further studies of preindustrial simulations may also help in understanding the evolution of sulfate aerosols from a pristine preindustrial era to present-day and future scenarios.

## References

- Albrecht, B. A. (1989), Aerosols, cloud microphysics, and fractional cloudiness, *Science*, 245, 1227–1230.
- Anderson, W. G., A. Ganadesikan, R. Hallberg, J. Dunne, and B. L. Samuels (2007), Impact of ocean color on the maintenance of the Pacific cold tongue, *Geophys. Res. Lett.*, 34, L11609, doi:10.1029/2007GL030100.
- Ayers, G. P., and J. L. Gras (1991), Seasonal relationship between cloud condensation nuclei and aerosol methanesulphonate in marine air, *Nature*, 353, 834–835, doi:10.1038/353834a0.
- Ayers, G. P., J. P. Ivey, and R. W. Gillett (1991), Coherence between seasonal cycles of dimethyl sulphide, methanesulphonate and sulphate in marine air, *Nature*, 349, 404–406, doi:10.1038/349404a0.
- Ballabriga-Poy, J., R. Murtugudde, R.-H. Zhang, and A. J. Busalacchi (2007), Coupled ocean–atmosphere response to seasonal modulation of ocean color: Impact on interannual climate simulations, *J. Clim.*, 20, 353–373.
- Bates, T. S., and P. K. Quinn (1997), Dimethylsulphide (DMS) in the equatorial Pacific Ocean (1982–1996): Evidence of a climate feedback?, *Geophys. Res. Lett.*, 24, 861–864.
- Bates, T. S., B. J. Huebert, J. L. Gras, F. B. Griffiths, and P. A. Durkee (1998), International Global Atmospheric Chemistry (IGAC) project's first Aerosol Characterization Experiment (ACE 1): Overview, *J. Geophys. Res.*, 103(D13), 16,297–16,318, doi:10.1029/97JD03741.
- Behrenfeld, M. J., et al. (2001), Biospheric primary production during an ENSO transition, *Science*, 291, 2594–2597.
- Boucher, O., et al. (2003), DMS atmospheric concentrations and sulphate aerosol indirect radiative forcing: A sensitivity study to the DMS source representation and oxidation, *Atmos. Chem. Phys.*, 3, 49–65, doi:10.5194/acp-3-49-2003.
- Cameron-Smith, P., J.-F. Lamarque, P. Connell, C. Chuang, and F. Vitt (2006), Toward an Earth system model: Atmospheric chemistry, coupling, and petascale computing, *J. Phys.: Conf. Ser.*, 46, 343–350, doi:10.1088/1742-6596/46/1/048.
- Cameron-Smith, P., S. Elliott, M. Maltrud, D. Erickson, and O. Wingenter (2011), Changes in dimethyl sulfide oceanic distribution due to climate change, *Geophys. Res. Lett.*, 38, L07704, doi:10.1029/2011GL047069.
- Carslaw, K. S., et al. (2013), Large contribution of natural aerosols to uncertainty in indirect forcing, *Nature*, 503(7474), 67–71, doi:10.1038/nature12674.

## Acknowledgments

This research was supported by NSF AGS1048995 and by DOE DE-SC0006679 as part of the U.S. Department of Energy, Office of Science, Biological and Environmental Research, Decadal and Regional Climate Prediction using Earth System Models (EaSM) program. The Pacific Northwest National Laboratory is operated for the DOE by Battelle Memorial Institute under contract DE-AC05-76RL01830. SE was supported by the Department of Energy ACME, HiLAT, and Benchmarking-Feedbacks Earth System Modeling projects within the Office of Biology and Environmental Science. P.C. was supported by the Scientific Discovery through Advanced Computing (SciDAC) program funded by U.S. Department of Energy, Office of Science, Advanced Scientific Computing Research and Biological and Environmental Research and performed under the auspices of LLNL under contract DE-AC52-07NA27344. The simulations used the supercomputing resources of the Office of Science of the U.S. Department of Energy at the National Center for Computational Sciences at Oak Ridge National Laboratory, under contract DE-AC05-00OR22725 and National Energy Research Scientific Computing Center under contract DE-AC02-05CH11231. We are grateful for atmospheric DMS measurements aboard the NOAA ship Discoverer taken by Timothy Bates of NOAA PMEL and taken in Cape Grim and Macquarie Island during the ACE-1 campaign provided by NCAR/EOL under the sponsorship of the National Science Foundation (<http://data.eol.ucar.edu/>) and those taken in Pacific Ocean provided by the UCI Saltzman/Aydin research group (<http://www.ess.uci.edu/researchgrp/esaltzman/data/>). L.X. thanks Xiaohong Liu of University of Wyoming and Minghuai Wang of Nanjing University in China for useful discussions on sulfur budgets presented in this work. All model simulations and the codes to produce the results shown here are available at <http://portal.nersc.gov/project/m1374/DMS/> from the National Energy Research Scientific Computing Center (NERSC).

- Chameides, W. L., and A. W. Stelson (1992), Aqueous-phase chemical processes in deliquescent sea-salt aerosols: A mechanism that couples the atmospheric cycles of S and sea salt, *J. Geophys. Res.*, 97, 20,565–20,580, doi:10.1029/92JD01923.
- Charlson, R. J., J. E. Lovelock, M. O. Andreae, and S. G. Warren (1987), Oceanic phytoplankton, atmospheric sulphur, cloud albedo and climate, *Science*, 236, 655–661, doi:10.1038/326655a0.
- Chavez, F. P., P. G. Strutton, and M. J. McPhaden (1998), Biological-physical coupling in the equatorial Pacific during the onset of the 1997–98 El Niño, *Geophys. Res. Lett.*, 25, 3543–3546, doi:10.1029/98GL02729.
- Chavez, F. P., P. G. Strutton, G. E. Friederich, R. A. Feely, G. C. Feldman, D. G. Foley, and M. J. McPhaden (1999), Biological and chemical response of the equatorial Pacific Ocean to the 1997–98 El Niño, *Science*, 286, 2126–2131.
- Dentener, F., et al. (2006), Emissions of primary aerosol and precursor gases in the years 2000 and 1750 prescribed data-sets for AeroCom, *Atmos. Chem. Phys.*, 6, 4321–4344, doi:10.5194/acp-6-4321-2006.
- Deser, C., A. S. Phillips, R. A. Tomas, M. Ohba, Y. M. Okumura, M. A. Alexander, A. Capotondi, J. D. Scott, and Y.-O. Kwon (2012), ENSO and Pacific decadal variability in Community Climate System Model version 4, *J. Clim.*, 25, 2622–2651, doi:10.1175/JCLI-D-11-00301.1.
- Elliott, S. (2009), Dependence of DMS global sea-air flux distribution on transfer velocity and concentration field type, *J. Geophys. Res.*, 114, G02001, doi:10.1029/2008JG000710.
- Gabric, A. J., R. Cropp, G. P. Ayers, G. McTainsh, and R. Braddock (2002), Coupling between cycles of phytoplankton biomass and aerosol optical depth as derived from SeaWiFS time series in the Subantarctic Southern Ocean, *Geophys. Res. Lett.*, 29(7), 1112, doi:10.1029/2001GL013545.
- Gabric, A. J., B. Qu, L. Rotstain, and J. M. Shephard (2013), Global simulations of the impact on contemporary climate of a perturbation to the sea-to-air flux of dimethylsulfide, *Aust. Meteorol. Oceanogr. J.*, 63(3), 365–376.
- Gondwe, M., M. Krol, W. Gieskes, W. Klaassen, and H. de Baar (2003), The contribution of ocean-leaving DMS to the global atmospheric burdens of DMS, MSA, SO<sub>2</sub>, and NSS SO<sub>4</sub>=, *Global Biogeochem. Cycles*, 17(2), 1056, doi:10.1029/2002GB001937.
- Harvey, M. (2007), The iron CLAW, *Environ. Chem.*, 4(6), 396–399.
- Hurrell, J. W., et al. (2013), The Community Earth System Model: A framework for collaborative research, *Bull. Am. Meteorol. Soc.*, 94, 1339–1360, doi:10.1175/BAMS-D-12-00121.
- Jochum, M., S. Yeager, K. Lindsay, K. Moore, and R. Murtugudde (2010), Quantification of the feedback between phytoplankton and ENSO in the community climate system model, *J. Clim.*, 23, 2916–2925.
- Kettle, A. J., and M. O. Andreae (2000), Flux of dimethyl sulfide from the oceans: A comparison of updated data sets and flux models, *J. Geophys. Res.*, 105, 26,793–26,808, doi:10.1029/2000JD900252.
- Kloster, S., J. Feichter, E. Maier-Reimer, K. D. Six, P. Stier, and P. Wetzel (2006), DMS cycle in the marine ocean-atmosphere system: A global model study, *Biogeosciences*, 3, 29–51.
- Lamarque, J.-F., et al. (2012), CAM-chem: Description and evaluation of interactive atmospheric chemistry in the Community Earth System Model, *Geosci. Model Dev.*, 5, 369–411, doi:10.5194/gmd-5-369-2012.
- Lana, A., et al. (2011), An updated climatology of surface dimethylsulfide concentrations and emission fluxes in the global ocean, *Global Biogeochem. Cycles*, 25, GB1004, doi:10.1029/2010GB003850.
- Le Clainche, Y., et al. (2010), A first appraisal of prognostic ocean DMS models and prospects for their use in climate models, *Global Biogeochem. Cycles*, 24, GB3021, doi:10.1029/2009GB003721.
- Lengaigne, M., C. Menkes, O. Aumont, T. Gorgues, L. Bopp, J.-M. André, and G. Madec (2007), Influence of the oceanic biology on the tropical Pacific climate in a coupled general circulation model, *Clim. Dyn.*, 28, 503–516.
- Leonard, C. L., and C. R. McClain (1996), Assessment of interannual variation (1979–1986) in pigment concentrations in the tropical Pacific using the CZCS, *Int. J. Remote Sens.*, 17, 721–732.
- Lewis, M. R., M.-E. Carr, G. C. Feldman, W. Esias, and C. McClain (1990), Influence of penetrating solar radiation on the heat budget of the equatorial Pacific, *Nature*, 347, 543–546.
- Liu, X., J. E. Penner, and M. Herzog (2005), Global modeling of aerosol dynamics: Model description, evaluation, and interactions between sulfate and nonsulfate aerosols, *J. Geophys. Res.*, 110, D18206, doi:10.1029/2004JD005674.
- Liu, X., et al. (2012), Toward a minimal representation of aerosols in climate models: Description and evaluation in the Community Atmosphere Model CAM5, *Geosci. Model Dev.*, 5, 709–739, doi:10.5194/gmd-5-709-2012.
- Löptien, U., C. Eden, A. Timmermann, and H. Dietze (2009), Effects of biologically induced differential heating in an eddy permitting coupled ocean-ecosystem model, *J. Geophys. Res.*, 114, C06011, doi:10.1029/2008JC004936.
- Marandino, C. A., W. J. De Bruyn, S. D. Miller, and E. S. Saltzman (2007), Eddy correlation measurements of the air/sea flux of dimethylsulfide over the North Pacific Ocean, *J. Geophys. Res.*, 112, D03301, doi:10.1029/2006JD007293.
- Marandino, C. A., W. J. De Bruyn, S. D. Miller, and E. S. Saltzman (2009), Open ocean DMS air/sea fluxes over the eastern South Pacific Ocean, *Atmos. Chem. Phys.*, 9, 345–356, doi:10.5194/acp-9-345-2009.
- Mårtensson, E. M., E. D. Nilsson, G. de Leeuw, L. H. Cohen, and H.-C. Hansson (2003), Laboratory simulations and parameterization of the primary marine aerosol production, *J. Geophys. Res.*, 108(D9), 4297, doi:10.1029/2002JD002263.
- Marzeion, B., A. Timmermann, R. Murtugudde, and F.-F. Jin (2005), Biophysical feedbacks in the tropical Pacific, *J. Clim.*, 18, 58–70.
- Monahan, E., D. Spiel, and K. Davidson (1986), A model of marine aerosol generation via whitecaps and wave disruption, in *Oceanic Whitecaps and Their Role in Air–Sea Exchange*, pp. 167–174, D. Reidel, Norwell, Mass.
- Moore, J. K., S. C. Doney, and K. Lindsay (2004), Upper ocean ecosystem dynamics and iron cycling in a global three-dimensional model, *Global Biogeochem. Cycles*, 18, GB4028, doi:10.1029/2004GB002220.
- Morrison, H., and A. Gettelman (2008), A new two-moment bulk stratiform cloud microphysics scheme in the community atmosphere model, version 3 (CAM3). Part I: Description and numerical tests, *J. Clim.*, 21, 3642–3659.
- Ooki, A., K. Miura, and M. Uematsu (2003), The increase of biogenic sulfate aerosol and particle number in marine atmosphere over the Northwestern North Pacific, *J. Oceanogr.*, 59, 799–807, doi:10.1023/B:JOCE.0000009571.81193.5d.
- Pandis, S. N., L. M. Russell, and J. H. Seinfeld (1994), The relationship between DMS flux and CCN concentration in remote marine regions, *J. Geophys. Res.*, 99, 16,945–16,957, doi:10.1029/94JD01119.
- Park, S., and C. S. Bretherton (2009), The University of Washington shallow convection and moist turbulence schemes and their impact on climate simulations with the community atmosphere model, *J. Clim.*, 22, 3449–3469.
- Park, S., C. S. Bretherton, and P. J. Rasch (2014), Integrating Cloud Processes in the Community Atmosphere Model, Version 5, *J. Clim.*, 27, 6821–6856, doi:10.1175/JCLI-D-14-00087.1.
- Preunkert, S., M. Legrand, B. Jourdain, C. Moulin, S. Belviso, N. Kasamatsu, M. Fukuchi, and T. Hirawake (2007), Interannual variability of dimethylsulfide in air and seawater and its atmospheric oxidation by-products (methanesulfonate and sulfate) at Dumont d'Urville, coastal Antarctica (1999–2003), *J. Geophys. Res.*, 112, D06306, doi:10.1029/2006JD007585.

- Quaas, J., O. Boucher, and U. Lohmann (2006), Constraining the total aerosol indirect effect in the LMDZ and ECHAM4 GCMs using MODIS satellite data, *Atmos. Chem. Phys.*, 6, 947–955, doi:10.5194/acp-6-947-2006.
- Quinn, P. K., and T. S. Bates (2011), The case against climate regulation via oceanic phytoplankton sulphur emissions, *Nature*, 480, 51–56.
- Reade, L., S. G. Jennings, and G. McSweeney (2006), Cloud condensation nuclei measurements at Mace Head, Ireland, over the period 1994–2002, *Atmos. Res.*, 82, 610–621, doi:10.1016/j.atmosres.2006.02.017.
- Russell, L. M., S. N. Pandis, and J. H. Seinfeld (1994), Aerosol production and growth in marine boundary layer, *J. Geophys. Res.*, 99, 20,989–21,003, doi:10.1029/94JD01932.
- Six, K. D., S. Kloster, T. Ilyina, S. D. Archer, K. Zhang, and E. Maier-Reimer (2013), Global warming amplified by reduced sulphur fluxes as a result of ocean acidification, *Nat. Clim. Change*, 3(11), 975–978, doi:10.1038/nclimate1981.
- Spada, M., O. Jorba, C. Pérez García-Pando, Z. Janjic, and J. M. Baldasano (2013), Modeling and evaluation of the global sea-salt aerosol distribution: Sensitivity to size-resolved and sea-surface temperature dependent emission schemes, *Atmos. Chem. Phys.*, 13, 11,735–11,755, doi:10.5194/acp-13-11735-2013.
- Textor, C., et al. (2006), Analysis and quantification of the diversities of aerosol life cycles within AeroCom, *Atmos. Chem. Phys.*, 6, 1777–1813, doi:10.5194/acp-6-1777-2006.
- Timmermann, A., and F.-F. Jin (2002), Phytoplankton influences on tropical climate, *Geophys. Res. Lett.*, 29(23), 2104, doi:10.1029/2002GL015434.
- Twomey, S. (1974), Pollution and the planetary albedo, *Atmos. Environ.*, 8, 1251–1256.
- Vallina, S. M., and R. Simó (2007), Strong relationship between DMS and the solar radiation dose over the global surface ocean, *Science*, 315(5811), 506–508.
- Vallina, S. M., R. Simó, and M. Manizza (2007), Weak response of oceanic dimethylsulfide to upper mixing shoaling induced by global warming, *Proc. Natl. Acad. Sci. U.S.A.*, 104, 16,004–16,009, doi:10.1073/pnas.0700843104.
- Vogt, M., and Piss, P. S. (2009), Dimethylsulfide and climate, in *Surface Ocean-Lower Atmosphere Processes*, vol. 187, edited by C. L. Quéré and E. S. Saltzman, pp. 197–232, AGU, Washington, D. C., doi:10.1029/2008GM000790.
- Wang, M., S. Ghan, M. Ovchinnikov, X. Liu, R. Easter, E. Kassianov, Y. Qian, and H. Morrison (2011), Aerosol indirect effects in a multi-scale aerosol-climate model PNNL-MMF, *Atmos. Chem. Phys.*, 11, 5431–5455, doi:10.5194/acp-11-5431-2011.
- Wetzel, P., E. Maier-Reimer, M. Botzet, J. Jungclaus, N. Keenlyside, and M. Latif (2006), Effects of ocean biology on the penetrative radiation in coupled climate models, *J. Clim.*, 19, 3973–3987.
- Wilks, D. (2011), *Statistical Methods in the Atmospheric Sciences*, Academic Press, Burlington, Mass.
- Wolff, E. W., et al. (2006), Southern Ocean sea-ice extent, productivity and iron flux over the past eight glacial cycles, *Nature*, 440(7083), 491–496.
- Woodhouse, M. T., K. S. Carslaw, G. W. Mann, S. M. Vallina, M. Vogt, P. R. Halloran, and O. Boucher (2010), Low sensitivity of cloud condensation nuclei to changes in the sea-air flux of dimethyl-sulphide, *Atmos. Chem. Phys.*, 10, 7545–7559, doi:10.5194/acp-10-7545-2010.
- Xu, L., D. W. Pierce, L. M. Russell, A. J. Miller, R. C. J. Somerville, C. H. Twohy, S. J. Ghan, B. Singh, J. Yoon, and P. J. Rasch (2015), Interannual to decadal climate variability of sea salt aerosols in the coupled climate model CESM1.0, *J. Geophys. Res. Atmos.*, 120, 1502–1519, doi:10.1002/2014JD022888.
- Yang, Y., et al. (2016), Impacts of ENSO events on cloud radiative effects in preindustrial conditions: Changes in cloud fraction and their dependence on interactive aerosol emissions and concentrations, *J. Geophys. Res. Atmos.*, 121, 6321–6335, doi:10.1002/2015JD024503.
- Zender, C. S., H. Bian, and D. L. Newman (2003), The mineral dust entrainment and deposition (DEAD) model: Description and 1990s dust climatology, *J. Geophys. Res.*, 108(D14), 4416, doi:10.1029/2002JD002775.
- Zhang, G. J., and N. A. McFarlane (1995), Sensitivity of climate simulations to the parameterization of cumulus convection in the Canadian Climate Center general circulation model, *Atmos.-Ocean*, 33, 407–446.
- Zhang, R.-H., et al. (2009), Role of ocean biology-induced climate feedback in the modulation of El Niño–Southern Oscillation, *Geophys. Res. Lett.*, 36, L03608, doi:10.1029/2008GL036568.